

CO rotational line emission in very red carbon stars in the Magellanic Clouds

Downloaded from: https://research.chalmers.se, 2026-11-23 06:23 UTC

Citation for the original published paper (version of record):
Groenewegen, M., Nanni, A., Boyer, M. et al (2026). CO rotational line emission in very red carbon stars in the Magellanic Clouds. Astronomy and Astrophysics, 714.
http://dx.doi.org/10.1051/0004-6361/202661169

N.B. When citing this work, cite the original published paper.

research.chalmers.se offers the possibility of retrieving research publications produced at Chalmers University of Technology. It covers all kind of research output: articles, dissertations, conference papers, reports etc. since 2004. research.chalmers.se is administrated and maintained by Chalmers Library

(article starts on next page)

A&A, 714, A130 (2026)
https://doi.org/10.1051/0004-6361/202661169
© The Authors 2026

Astronomy & Astrophysics

CO rotational line emission in very red carbon stars in the Magellanic Clouds

M. A. T. Groenewegen[1,⋆], A. Nanni[2,3], M. L. Boyer[4], L. Decin[5], S. R. Goldman[4], K. Justtanont[6], F. Kerschbaum[7], I. McDonald[8], H. Olofsson[6], R. Sahai[9], G. C. Sloan[4,10], J. Th. van Loon[11], W. H. T. Vlemmings[6], and A. A. Zijlstra[8]

[1] Koninklijke Sterrenwacht van België, Ringlaan 3, 1180 Brussels, Belgium
[2] National Centre for Nuclear Research, ul. Pasteura 7, 02-093 Warsaw, Poland
[3] INAF – Osservatorio astronomico d'Abruzzo, Via Maggini SNC, 64100 Teramo, Italy
[4] Space Telescope Science Institute, 3700 San Martin Drive, Baltimore, MD 21218, USA
[5] Institute of Astronomy, Department of Physics and Astronomy, University of Leuven, Celestijnenlaan 200D, 3001 Leuven, Belgium
[6] Department of Physics and Astronomy, Chalmers University of Technology, 412 96 Gothenburg, Sweden
[7] Department of Astrophysics, University of Vienna, Türkenschanzstr. 17, 1180 Vienna, Austria
[8] Jodrell Bank Centre for Astrophysics, The University of Manchester, Oxford Road, Manchester, M13 9PL, UK
[9] Jet Propulsion Laboratory, California Institute of Technology, MS 183-900, Pasadena, CA 91109, USA
[10] Department of Physics and Astronomy, University of North Carolina, Chapel Hill, NC 27599-3255, USA
[11] Lennard-Jones Laboratories, Keele University, Staffordshire ST5 5BG, UK

Received 28 May 2026 / Accepted 10 August 2026

ABSTRACT

Stars of low and intermediate initial mass lose most of their stellar mass at the end of their lives during the asymptotic giant branch (AGB) phase. Determining their gas and dust mass-loss rates (MLRs) is crucial for quantifying the contribution of evolved stars to the life cycle of dust and gas in the Universe. The Atacama Large Millimeter/submillimeter Array was used to observe 38 carbon stars (C stars) in the large Magellanic cloud (LMC) and three C stars in the small Magellanic cloud (SMC) in the CO J= 2–1 line. Line profiles were fitted to derive stellar velocities and wind-expansion velocities ($V_{\rm exp}$). CO emission is detected in two C stars in the SMC and 33 C stars in the LMC, extending earlier work from 2016 that detected CO emission from a total of four C stars observed in the LMC. This is the first detection of carbon monoxide around an AGB star in the SMC. One object in the LMC shows emission in ^{13}CO. The wind-expansion velocity ranges from ∼7.5 to ∼30 km s^{-1}. Archival data were used to determine the pulsation periods as well as construct and model the spectral energy distributions using two dust radiative transfer codes. Mass-loss rates were independently derived from these two codes as well as from the intensity of the CO line, using a simple formula. On average, the dust-based MLRs higher than the MLRs based on the CO line by a factor of 1.6. Additional CO data in other transitions, combined with proper modelling, is required to further investigate this possible discrepancy. Mass-loss rates, pulsation periods, and expansion velocities were compared to a sample of Galactic C stars. There is a strong bias, as the Magellanic Cloud targets sample the highest MLRs and luminosities, yet they represent only a minority of stars in a Galactic sample. Comparing this sample with a similarly extreme set of Galactic stars with periods longer than 500 days, we identify no correlation between metallicity and either the MLR or $V_{\rm exp}$.

Key words. stars: AGB and post-AGB – stars: carbon – stars: mass-loss – Magellanic Clouds

1. Introduction

Low- and intermediate-mass stars (with initial masses of ∼0.8–8 M$_\odot$) end their lives with an intense mass-loss episode during the asymptotic giant branch (AGB) phase. The standard picture is that stellar pulsation and dust formation drive a slow, cool wind. This wind from AGB stars is one of the main sources that enriches the interstellar medium (ISM) with gas and dust (see Höfner & Olofsson 2018 for a review). Carbon (C) stars are a subset of AGB stars that underwent so many helium shell flashes (or thermal pulses), a process in which carbon (the product of He burning) mixes into the stellar envelope, that carbon atoms outnumber oxygen atoms (C/O > 1). The initial mass range of AGB stars that become C stars depends on metallicity, but is typically ∼1.5–4.0 M$_\odot$ (see e.g. Ventura et al. 2020, 2021).

The dust mass-loss rate (MLR) is typically modelled using the spectral energy distribution (SED), which requires a (dust) expansion velocity, that cannot be directly measured, and, therefore, must be estimated. The gas MLR is usually determined from the rotational transitions of carbon monoxide (CO), which includes a measurement of the expansion velocity obtained from the width of the line profile. Wind-expansion velocities ($V_{\rm exp}$) have been measured for hundreds of AGB stars in the Milky Way (MW) through either CO thermal line emission, typically using single-dish telescopes (see representative studies by e.g. Kerschbaum & Olofsson 1999; Olofsson et al. 2002; Groenewegen et al. 2002a; Kemper et al. 2003; De Beck et al. 2010; Ramstedt et al. 2020; Wallström et al. 2025) or OH maser line emission for O-rich sources (see the database by Engels & Bunzel 2015)[1].

⋆ Corresponding author: martin.groenewegen@oma.be

[1] https://hsweb.hs.uni-hamburg.de/projects/maserdb_new/

Open Access article, published by EDP Sciences, under the terms of the Creative Commons Attribution License (https://creativecommons.org/licenses/by/4.0), which permits unrestricted use, distribution, and reproduction in any medium, provided the original work is properly cited.
This article is published in open access under the Subscribe to Open model. Subscribe to A&A to support open access publication.

The first indication that the $V_{\rm exp}$ of AGB stars depends on environment (metallicity) was presented in Wood et al. (1992) based on OH/IR stars in the large Magellanic cloud (LMC). For C stars this began with the detection of CO (2–1) emission in the halo object IRAS 12560+1656 (Groenewegen et al. 1997), while Lagadec et al. (2010) detected CO J = 3–2 emission in this and five other C stars. The $V_{\rm exp}$ were lower than those of C stars in the Galactic disk, with a value as low as ∼3 km s^{-1} in IRAS 12560. Similar results have been derived for O-rich stars. McDonald et al. (2019) report a $V_{\rm exp}$ velocity of about 3.2 km s^{-1} in the metal-poor ([Fe/H]=−0.72) star 47 Tuc V3, while McDonald et al. (2020) find a $V_{\rm exp}$ = 3.5 km s^{-1} in the metal-poor ([Fe/H] = −1.3 to −1.0 dex) star RU Vul. These velocities are lower than that for typical O-rich AGB stars in the MW. Several factors may play a role, but one possibility is the lack of refractory material at lower metallicity. However, since carbon stars produce their own refractory material through the dredge-up of carbon produced during helium shell burning and thus therefore largely independent of the initial metallicity it has been unclear whether their winds are similarly slowed.

Hydrodynamical wind models by Bladh et al. (2019) predict MLR and $V_{\rm exp}$ for the small Magellanic cloud (SMC), LMC, and solar metallicities for a star with a current mass of 1 M$_\odot$ for a few effective temperatures, piston velocities, and carbon excesses. Based on the model outputs for 20 objects where data are available for all metallicities and for a piston velocity of 6 km s^{-1}, the MLR ratios are solar/LMC= 0.87 ± 0.02 and solar/SMC= 0.83 ± 0.02 (mean value and error on the mean). The $V_{\rm exp}$ ratios are solar/LMC= 0.96 ± 0.02 and solar/SMC= 0.96 ± 0.02. In other words, lower metallicities lead to slightly higher MLRs on average, exhibiting almost no dependence of $V_{\rm exp}$ on metallicity (cf. Fig. 7 in Bladh et al. 2019). Gas-to-dust (GTD) ratios are not reported for the individual models but their Fig. 8 suggests values between 500 and 6000, independent of metallicity.

Since maser emission is stronger than thermal emission, attempts have been made to detect OH emission in the SMC and LMC. Goldman et al. (2017) summarises the current state of affairs and presents accurate $V_{\rm exp}$'s for 13 OH/IR stars in the LMC. They suggest that $V_{\rm exp}$ is proportional to metallicity and luminosity as $L^{0.4}$. However, Goldman et al. (2018) still find no detections in the SMC.

Groenewegen et al. (2016) (hereafter Gr16) presented the first detections of spectrally resolved CO line emission in extragalactic stars, namely in the LMC. Four C stars were targeted and all were detected, while two OH/IR stars were observed with one marginal detection. A comparison was made to similarly highly red Galactic C stars, tentatively concluding that for C stars the $V_{\rm exp}$'s in the LMC are lower than in the solar neighbourhood, while the MLRs appear similar.

This paper presents observational results of a much larger sample of C stars both in the SMC and LMC to verify some of the preliminary conclusions of Gr16. Our selected list of targets is presented in the next section. ALMA observations are presented in Sect. 3. Selected observational results are presented in Sect. 4, including an analysis of the CO line profiles. The determination of the pulsation periods are discussed in Sect. 5, while the analysis of the SEDs and determination of the MLRs are presented in Sect. 6. The paper ends with a discussion (Sect. 7) and a summary, with conclusions presented in Section 8.

2. Targets

Targets were selected based on predictions of the CO line strength, which, in turn, were based on detailed dust modelling and a comparison with the results in Gr16. Dust models are available for ∼8000 C-rich AGB stars in the LMC and ∼3000 in the SMC, based on mid-IR photometry from the *Spitzer* SAGE survey (Nanni et al. 2018, 2019, hereafter N18 and N19). Models are also available for a subsample of ∼500 AGB and red supergiant (RSG) stars (including O-rich AGB stars), based on mid-infrared spectra from the IRS on board *Spitzer* as well as from complete SEDs (Groenewegen & Sloan 2018).

In the N18 and N19 models (also see Sect. 6.2), the growth of dust grains of different chemical compositions in the circumstellar envelopes (CSEs) of thermally pulsing AGB (TP-AGB) stars is coupled with a spherically symmetric, stationary wind (Nanni et al. 2013, 2014 and references therein). Applying this calculation to stellar evolutionary tracks reproduces the observed trend between the ($V_{\rm exp}$) and MLR of Galactic C stars well (Nanni et al. 2013). Dust radiative transfer (RT) calculations are performed a posteriori to compute the spectra as reprocessed by the dust using the code MORE OF DUSTY (MoD) (Groenewegen 2012; Ivezić et al. 1999).

This approach allows one to consistently compute the dust-production rate (DPR), the GTD ratio, and $V_{\rm exp}$ as well as the MLRs of the fitted stars. The values obtained for the GTD ratio are comparable with results from detailed hydrodynamical calculations (Mattsson et al. 2010; Eriksson et al. 2014).

Based on the modelling results in N18 and N19, the CO-integrated intensities and peak line intensities were predicted using multi-parameter fits (De Beck et al. 2010), assuming parabolic CO profiles and the predicted values for $V_{\rm exp}$. Standard distances of 50 kpc for the LMC and 60 kpc for the SMC were assumed. The predictions are relative intensities, as they also depend on the beam size and the CO/H_2 abundance. These relative intensities were compared to the peak fluxes and integrated intensities for the four C stars detected in CO(2–1) by Gr16. This comparison lead to a scaling factor, accurate to within a factor of 2, which enables us to select stars detectable with high certainty. In addition, the formalism in De Beck et al. (2010) showed that the most efficient way to detect the CO line and determine the expansion velocity is via observations of the J=2–1 transition. The 1–0 transition is weaker than 2–1. The 3–2 line is slightly stronger; nonetheless, it is not strong enough to compensate for the less favourable atmospheric transmission.

The initial sample was restricted to C stars with a predicted CO(2–1) intensity greater than 20 mJy (i.e. half the intensity of IRAS 05506−7053 in Gr16). This sample was then further refines to cover a range of predicted $V_{\rm exp}$, GTD ratios, L, and MLR, as well as to ensure the availability of IRS spectra and pulsation periods.

The final sample consists of three SMC and 38 LMC C stars. Combined with the four C stars in Gr16, this represents only 0.5 percent of the total estimated population of C stars in the LMC. Nevertheless, the combined MLRs of these stars is estimated to be 8 ×10^{-4} M$_\odot$ yr^{-1} (or 2.3 ×10^{-6} M$_\odot$ yr^{-1} in dust), or ∼6% of the total gas and 16% of the total dust returned by the entire population (Nanni et al. 2019). This indicates the importance of studying in detail this representative sample of the reddest stars.

To quantify the redness of our sample, we note that Boyer et al. (2011) in their study of evolved stars in the LMC observed with *Spitzer* found 25 914 objects with detections in the [3.6] and [4.5] bands (excluding red giant branch (RGB) and RSGs). The LMC star in our sample with the bluest colour has [3.6–4.5] = 0.37; the second bluest has 0.61, and the reddest colour is 3.3 mag. In the non-RGB and non-RSG samples of Boyer et al. (2011) 1016 objects have [3.6–4.5] > 0.37 mag, corresponding

Table 1. ALMA SGs and general properties.

SG	Observation dates	EB	T (h:m)	N_{Tel}	Baselines (m)	N_{obj}	Beam ($'' \times ''$)
SMC	2024-01-01 21:36–2024-01-02 00:49	3	1:49	46	15–784	3	0.585×0.496
LMC strong	2024-01-02 05:14–2024-01-02 01:55	2	1:75	46, 49	15–784	16	0.570×0.516
LMC weak	2024-01-04 03:26–2024-05-24 18:55	11	8:52	41, 43, 44, 46, 47	15–(284,312,500,740,784)	22	0.826×0.654

Notes. Listed are the name of the science goal, range in observation dates, number of execution blocks, total time on target, the number of telescopes used, the range in baselines, the number of science targets, and the typical size of the reconstructed beams.

to approximately 4%. Our stars are chosen to be carbon stars, so restricting the Boyer et al. (2011) sample to the relevant classes of C-AGB, x-AGB and FIR, this ratio becomes 992 out of 8761 objects. Our sample of very red C stars, therefore, represents about the reddest 10% of the known and likely C stars in the LMC.

3. Observations and post-processing of the data

The predicted CO strengths cover a range in intensities, and we therefore decided to split the observations into three science goals (SGs): one for the SMC stars, one for the LMC stars predicted to have weaker emission (called LMC weak or LMCwk), and one for the LMC stars predicted to have stronger emission (called LMC strong or LMCst). For the first two SGs an rms noise level of 3 mJy was requested. For the third SG, the requested noise level was 6 mJy.

The sources were observed with ALMA at Band 6 in early 2024. Table 1 provides the details of the observations as well as the typical size of the reconstructed beams. The average on-source integration time was 7 minutes for LMCst and 24 minutes for the other two SGs.

The observations had four spectral windows (SPWs): one with a width of 937.5 MHz and 1920 channels to cover the ^{12}CO(2–1) transition centred on 230.538 GHz, one window with the same spectral set-up to cover the ^{13}CO(2–1) transition centred on 220.399 GHz, and two 1.875 GHz windows with 240 channels each for the continuum centred on 219.00 and 232.80 GHz, respectively. The channel spacing in the line SPWs was about 0.64 km s^{-1} corresponding to an effective spectral resolution of about 0.74 km s^{-1}. The image cell size was 0.120″ for the LMCwk SG, and 0.096″ for the two other SGs.

Pipeline products were retrieved from the ALMA archive that had been processed using the Common Astronomy Software Applications (CASA, version 6.5.4.9) pipeline (McMullin et al. 2007). The quality control log files indicated that self-calibration was attempted but not applied due to the low signal-to-noise. Post-processing was done on local computers using the same version of CASA.

The first step in the post-processing aimed at determining the source position and shape of the source based on the ^{12}CO data. A zero-moment map was created using channels 800–1200 (covering ~95 to ~378 km s^{-1}) for the LMC sources and channels 700–1100 (covering ~50 to ~305 km s^{-1}) for the SMC sources, corresponding to the expected range in velocities showing emission. A rectangular region of 41 pixels wide (about 4–5″×4–5″) placed in the centre of the moment map was defined and a two-dimensional Gaussian fit was performed resulting in the position of the source (with error bars) and the major and minor axis and position angle (with error bars) of the Gaussian. It was verified a-posteriori that the input coordinates based on SAGE IR data matched very well with the ALMA position, with a difference of at most 0.5″, and a median difference of 0.20″ among 35 detections, so that the sources are indeed expected to be located in the centre of the image.

The next step was to extract the ^{12}CO line spectrum. The size of the region, from which the spectrum was extracted, was set by the (maximum) expected size of the CO emitting region. The photo dissociation radius $r_{\frac{1}{2}}$, defined as the radius where half the CO is dissociated, is larger for higher MLRs, lower V_{exp}, and larger f_{CO/H_2} values. The largest value in the grid of Saberi et al. (2019) is about 1.1×10^{18} cm for an expansion velocity of 7.5 km s^{-1}, $\dot{M}$= 1×10^{-4} M$_\odot$ yr^{-1} and f_{CO/H_2}=10×10^{-4}. At 50 kpc this implies a (maximum) CO shell size of about 1.4″. For an expansion velocity of 15 km s^{-1}, $\dot{M}$= 2×10^{-5} M$_\odot$ yr^{-1}and f_{CO/H_2}= 8×10^{-4}, it is already 3.5 times smaller. About half of the sources have predicted MLRs in the range 2–4 $\times$ 10^{-5} M$_\odot$ yr^{-1}, based on N18 and N19. As we discuss deriving MLR estimates later in the analysis, one could fine-tune this aperture on a source-by-source basis; however, this would introduce large uncertainties. Therefore we chose to adopt a conservative large aperture size. Given a spatial full-width half-maximum (FWHM) major axis of the beam of (at most) 0.83″ and a maximum photo dissociation radius of 1.4″, the line flux was extracted inside a circle with radius 2.0″. This aperture should cover the line-emitting region in all the objects and is centred on the pixel coordinates of the object. A Gaussian fit was made to the profile to obtain a peak velocity estimate and the FWHM width of the profile.

In a third step, the ^{13}CO(2–1) profile was extracted. Anticipating that all but one source would be non-detections, the velocity range of the ^{12}CO profile was converted to the range of channels in the ^{13}CO SPW, and the line was extracted within the aforementioned spatial region.

The fourth step involved determining the dust-continuum emission in the line-free SPWs. The four SPWs were treated separately. For each SPW, a −1st moment map was created (i.e. giving the average value along the spectral axis), excluding the channels with emission. Although only one source was clearly detected in ^{13}CO, the expected spectral region for the ^{13}CO emission was excluded in all stars based on the spectral range of the ^{12}CO detection. The region where the dust emission can occur is larger than the CO-emitting region. Based on the RT calculations mentioned in Sect. 2, the outer radius of the dust shell, where the dust temperature becomes 20 K is about 4.5″ at the distance of the LMC for the objects with the largest predicted MLRs. The continuum emission was extracted from a circular region of radius r_{source}= 4.5″ centred on the source (about 38 pixels). As for the aperture to derive the CO emission, one might fine-tune the aperture to estimate the continuum emission on a source-by-source basis. We, nevertheless, chose to adopt a conservative large aperture size for all sources.

An off-source region was defined as a circle with an inner and outer radius that are (arbitrarily) 4 and 24 pixels larger than $r_{\rm source}$. From that region, the rms noise was extracted (the median absolute deviation times 1.483[2] was actually used as a more robust estimate of the noise level), and the error in the flux in the on-source region was determined.

This procedure produces four estimates of the continuum flux with error bars at four wavelengths, typically ranging between 1290 and 1370 μm. From the RT calculation, the flux from C stars at millimetre wavelengths is expected to follow λ^{-2}; therefore, the four flux estimates were scaled to a wavelength of 1330 μm. Then, the weighted average and the error in the mean were calculated. If the flux was less than three times the error bar, the 3σ upper limit was quoted.

Finally, a $10''\times10''$ cut-out of the ^{12}CO region was produced, based on the zeroth moment image (see Appendix A). This step was made in a second iteration, where the fixed range in the channels was replaced with a range in velocity centred on the detected line (when detected).

4. Observational results

4.1. Analysis of the line profiles

The line profiles were fitted with a 'Shell' profile as defined in the CLASS/GILDAS software package[3]:

$$P(V) = \frac{A}{\Delta V\ (1+H/3)} \left(1 + 4H \left(\frac{V-V_\star}{\Delta V}\right)^2\right), \quad (1)$$

where $V_\star$ is the stellar velocity (in km s^{-1}; throughout the paper the Local Standard of Rest (LSR) frame is used), A is the integrated intensity (in Jy km s^{-1}), ΔV the full-width at zero intensity (in km s^{-1}; $V_{\rm exp}$ is taken as half that value), and H is the horn-to-centre parameter. This parameter describes the shape of the profile. It is -1 for a parabolic profile, 0 for a flat-topped one, and > 0 for a double-peaked profile. H was fixed to -1 in the fitting. A parabolic profile indicates optically thick, unresolved emission. Leaving H as a free parameter typically gives a value with a large error bar consistent with -1. Table E.1 lists the results and all profiles are shown in Appendix B.

Error bars on $V_\star$ and ΔV are based on Monte Carlo simulations, in which simulated spectra were generated by using a Gaussian distribution of the errors and subsequently re-fitting the profile. The quoted parameters represent the median value, with the error bars given by the difference between the 69% and 31% percentiles. Upper limits are based on the 97.3% percentile (i.e. 3σ values). In the case of the non-detected ^{13}CO lines, the expansion velocity was fixed to the value derived from the ^{12}CO profile, and the systemic velocity was allowed to vary within the width of the ^{12}CO profile. In the case of ^{12}CO non-detections, the upper limit to the intensity was derived by fixing $V_{\rm exp}$ to 9 km s^{-1} for the SMC and 15 km s^{-1} for the LMC sources (the typical values among the detections) and allowing the stellar velocity to vary relative to an arbitrary initial value.

4.2. Non-detections

Thirty-five out of forty-one objects were detected. For one of the three SMC and five of the 38 LMC sources, no convincing ^{12}CO profile could be derived. For four objects (SAGE MCJ045344, MSX LMC 1220, MSX LMC 474, and MSX LMC 527) the images in Appendix A appear to show a possible source close to the centre; however, the spectra (Figure B.1) revealed no line, even after they were binned in velocity space.

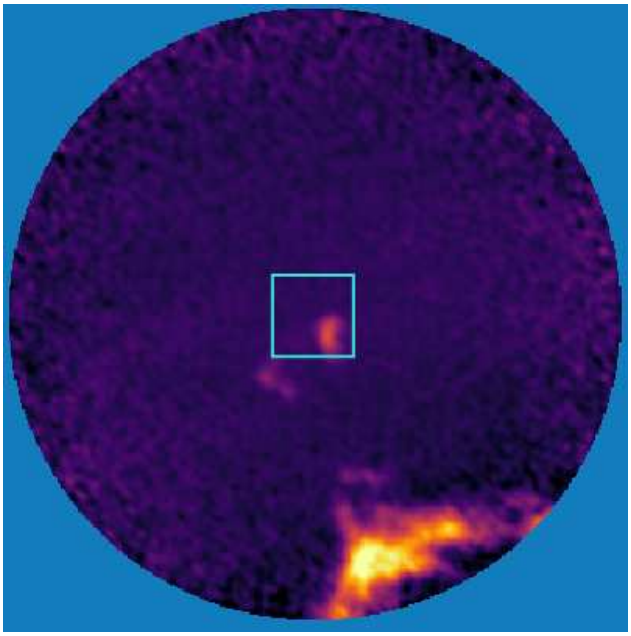

Fig. 1. Emission in five spectral channels in the field around MSX LMC 527 (about 36″ across). The box in the centre measures about 5″ per side and is centred on the nominal source position.

The observation of MSX LMC 527 is contaminated by emission from the ISM. Figure 1 shows an hourglass structure unrelated to the object. The emission is extremely narrow (five channels or about 3 km s^{-1}) and much stronger than any of the other detections. The CO profile shown in Figure B.1 excludes these channels, and no obvious underlying emission related to the AGB star is visible. Other ISM emission appear in the field at these velocities, which also indicates that this emission is not centred on the expected source position.

Interstellar medium contamination also occurs in the detected source MSX LMC 1780, where seven channels have been removed in the profile shown in Figure B.1. The removal of these channels did not impact the derivation of the parameters of the profile. In the cases of SAGE MCJ045344, MSX LMC 1220, and MSX LMC 474, ISM contamination does not seem to play a role. Observations with better sensitivity, or the use of a prior on stellar velocity (e.g. from infrared spectroscopy), could reveal the CO profile of the AGB star or yield a more stringent upper limit.

4.3. The ^{13}CO detection

One of the targets is detected in ^{13}CO, the LMC carbon star IRAS 05568 (see Fig. B.1). The ratio of the integrated intensities is ^{12}CO/^{13}CO = 1.8 ± 0.1. The ^{12}CO is likely optically thick, as indicated by the parabolic line shape; therefore, the ^{12}C/^{13}C ratio is likely larger but probably not by a huge factor. To quantify this, full RT modelling would be required. The ^{12}C/^{13}C ratio is similar to that observed in J-type C stars (4–10, Abia & Isern 2000 close to the CN cycle equilibrium value of 3). J-type C stars are not rare in the MW and LMC (10–15%; Abia & Isern 2000; Morgan et al. 2003) but the J-type character or quantitative abundance

[2] This gives the 1σ value in a Gaussian distribution.

[3] https://www.iram.fr/IRAMFR/GILDAS/doc/html/class-html/node38.html

analysis has been done exclusively based on optical spectra so far. This observation is the first indication of the J-type nature of an LMC C star with a high MLR, and the second object after the galactic object IRAS 15194−5115 (^{12}CO/^{13}CO = 6, Woods et al. 2003). Among the ^{13}CO non-detections, the most stringent lower limits come from stars where the ^{12}CO is strong, ^{12}CO/^{13}CO $\gtrsim$ 15–19 (IRAS 05416, TRM 74, and IRAS 05190).

5. Pulsation periods

Time-series data for the objects were obtained from the VISTA Magellanic Cloud (VMC) survey (Cioni et al. 2011) Data Release (DR) 6 in the K band as well as the Wide-field Infrared Survey Explorer (WISE) and Near-Earth Object WISE (NEOWISE) surveys (Wright et al. 2010; Mainzer et al. 2011, 2014) in the W1 and W2 bands (centred at 3.4 and 4.6 μm, respectively).

From the AllWISE multi-epoch photometry table and the NEOWISE-R single-exposure source table[4], all entries within 1″ of the source coordinates were downloaded in the W1 and W2 filters, with the additional constraint that the error bars on the magnitudes were <0.25 mag and the flags *saa_sep* > 5 and *moon_masked* = 0 (e.g. Uchiyama & Ichikawa 2019) were applied.

At the bright end, the WISE and NEOWISE data suffer from saturation that influences the photometry; thus, a correction was applied. Table 2 in Sect. II.1.c.iv.a of the NEOWISE Explanatory Supplement[5] contains correction tables in the W1 and W2 filters for all phases of the mission. At the bright end (fourth mag) the corrections are about 0.06 and 0.4 mag in the WISE W1 and W2 filters and 0.7 and 0.9 mag in the NEOWISE W1 and W2 filters. These corrections reach low (0.02 mag) levels at 6.8 and 6.0 mag (WISE W1 and W2) as well as 6.9 and 7.9 mag (NEOWISE W1 and W2), respectively.

The light curves (LCs) were pre-analysed with the code PERIOD04 (Lenz & Breger 2005) to estimate the period. With this initial guess for the period, a function,

$$m(t) = m_0 + A\sin(2\pi\ t\ e^f) + B\cos(2\pi\ t\ e^f), \quad (2)$$

was fitted to the LC using the weighted linear least-squares fitting routine MRQMIN, assuming a single dominant period for simplicity. Fitting was performed with the Fortran codes available in *Numerical Recipes* (Press et al. 1992), as described in Appendix A of Groenewegen (2004), and modified to analyse VMC K-band data and WISE/NEOWISE data, as described in Groenewegen et al. (2020); Groenewegen (2022). The resulting parameters are listed in Tables C.1 and C.2 for the VMC and WISE data, respectively. These include the mean magnitudes (m_0), the period (exp($-f$)), and amplitude ($\sqrt{A^2+B^2}$) with their associated uncertainties. Figures C.1 and C.2 provide examples of the LCs and the fits, and the full set is available through Zenodo. The periods derived in the present paper supersede those reported in Gr16 for IRAS 05506, IRAS 05125, ERO 0529379, and ERO 0518117, as they are based on additional data. Table E.2 lists the adopted period in the last column. This is determined as the weighted mean (and the error on the mean) of the available periods. The column is empty when the period is larger than 2500 d, the amplitude is smaller than 0.2 mag, or when the error on the amplitude is greater than $\frac{1}{3}$ of its value.

[4] see https://irsa.ipac.caltech.edu/cgi-bin/Gator/nph-scan?mission=irsa&submit=Select&projshort=WISE

[5] http://wise2.ipac.caltech.edu/docs/release/neowise/expsup/sec2_1civa.html

6. SED fitting and mass-loss rates

Two sets of RT dust models have been used, as described in the following sections. Both have complementary approaches, in order to better appraise uncertainties in the derived parameters.

6.1. More of DUSTY models

More of Dusty models were run using the 'density type = 3' mode, in which the hydrodynamical equations of dust and gas are solved and the gas-expansion velocities and gas MLRs are predicted (following Gr16).

Inputs to the RT model include atmosphere models from Aringer et al. (2009) and a combination of amorphous carbon (AMC), silicon carbide (SiC), and magnesium sulphide (MgS) dust. Details are given in Appendix D.

The RT models were fitted to broad-band photometry (compiled in Table D.1) and *Spitzer* IRS spectra (see Groenewegen & Sloan 2018 for details), when available. The fitted parameters include luminosity, dust optical depth (τ_d at 0.5 μm), and the dust temperature at the inner radius, T_c. The outer radius was set to 3000 times the inner radius. The velocities and MLR, given by DUSTY, scale as

$$V_{\rm exp} \sim (L/10^4)^{0.25}\left((r_{\rm gd}/200)(\rho_{\rm d}/3)\right)^{-0.5} \text{ and}$$

$$\dot{M} \sim (L/10^4)^{0.75}\left((r_{\rm gd}/200)(\rho_{\rm d}/3)\right)^{+0.5}, \text{ respectively,}$$

where L is the luminosity in solar units, $r_{\rm gd}$ is the GTD ratio, and $\rho_{\rm d}$ is the specific density of the dust grains in g cm^{-3}.

The GTD ratio was first tuned to fit the observed expansion velocity (taking the specific density for the adopted dust species of that source), and then used with the fitted luminosity to derive the MLR. The error on the GTD ratio was calculated accounting for the error in $V_{\rm exp}$ and L. The error in the MLR accounts for the error in the GTD ratio, the error in the dust optical depth, and the error in luminosity. Additional uncertainties are hard to account for, which relate to differences in grain optical properties and grain densities. Fitting results are listed in Columns 7–10 in Table E.2. Examples fits to the SEDs are discussed in Sect. 6.3 and shown in Fig. D.1.

6.2. Nanni models

Second, for the SED fitting, we adopted the grids of models presented in N18 and N19 initially used to predict the intensities described in Sect. 2. In these models, dust formation is self-consistently computed throughout the CSE of the star, coupled with stationary wind, given the stellar input parameters (e.g. current stellar mass, effective temperature, luminosity, MLR, and photosphere element abundances), as fully described in Nanni et al. (2013, 2014) (see Appendix D).

The models predict $V_{\rm exp}$, the GTD ratio, the dust temperature at the inner boundary of the CSE as well as the dust density profile. These outputs of the calculation were adopted as inputs to the MoD code to compute the spectra reprocessed by dust as a function of the stellar parameters. The adopted model parameters were selected to have predicted $V_{\rm exp}$'s within 3σ of the observed values, while all the input parameters were free to vary. The fitting results are listed in Columns 2–6 of Table E.2.

A comparison between the MoD and the Nanni models is presented in Appendix D. The geometric mean of the independent model calculations was adopted, and the values are given in Columns 11–13 in Table E.2.

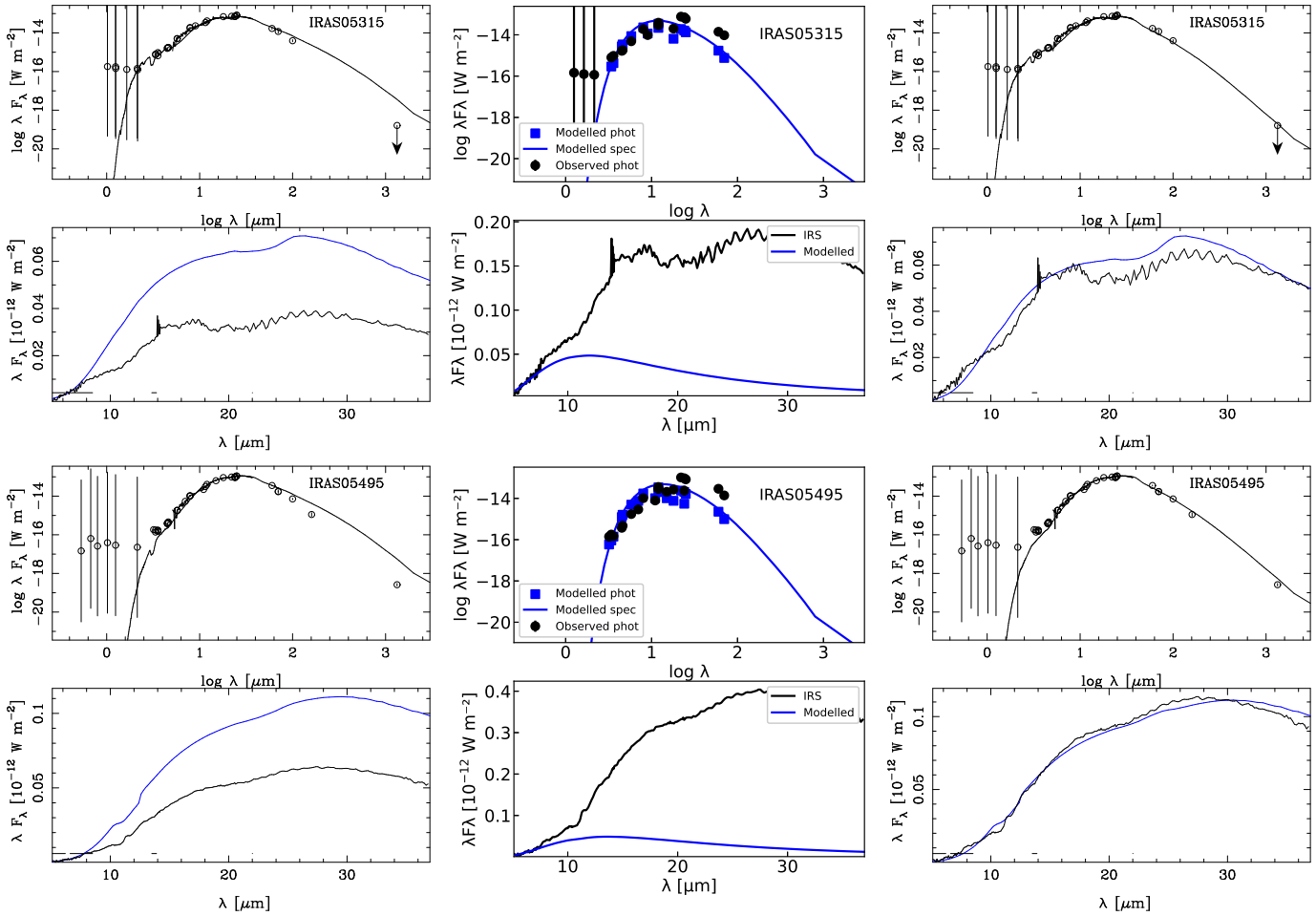

Fig. 2. Standard SED fits from the MoD (left) and Nanni (middle panel) models, and a MoD model with an adopted density law ($r^{-2.5}$) tuned to fit the ALMA continuum at 1330 µm (right panel) for IRAS 05315 (top row) and IRAS 05495 (bottom row). See Sect. 6.3 for details.

6.3. SED fit results and ALMA continuum data points

Examples fits to the SEDs from the two models are shown in Fig. D.1. The comparison can be considered acceptable in some cased, such as for MSX LMC 527 and IRAS 06018 in Fig. D.1, given that the two models have fundamentally different approaches (see discussion in Appendix D). However, it is poor in other cases (e.g. IRAS 05315).

It is illustrative to discuss the cases comparing the observed versus predicted ALMA 1330 µm continuum. For 32 objects an upper limit was derived, and in 27 cases the MoD model indeed falls below the upper limit, such as for MSX LMC 527 and IRAS 06018. In three cases the discrepancy is deemed acceptable (within a factor of 2; e.g. IRAS 05568), but for two cases the difference is large (TRM 74 and IRAS 05315). Among the nine detections, the model agrees very well with the observations for one source (IRAS 05133) and predicts somewhat lower fluxes for six sources. However, in one case (IRAS 05495) the model significantly overestimates the flux.

IRAS 05315 and IRAS 05495 are good illustrations of how different assumptions in the MoD and Nanni models lead to very different results. They likewise illustrate that the standard MoD model fails to fit the ALMA dust continuum observation (see Fig. 2). In the Nanni models, the dust temperature at the inner radius reflects the dust condensation process, and the temperature is of the order of 950 K for these two objects. In the MoD models, this temperature is a free parameter and is found to be low (around 300 K). In the Nanni models, the best fit under-predicts the mid-IR flux, while the MoD model provides a slightly better overall fit but over-predicts the mid-IR and millimetre fluxes.

One way of lowering the millimetre flux is to have less dust than that predicted by the radiation-driven wind model where the dust density follows r^{-2} from the point where the terminal wind velocity is reached. The right-hand panels of Fig. 2 present models with a $r^{-2.5}$ dependence. They clearly yield much-improved fits but result in current MLRs (i.e. at the dust inner radius) that are significantly higher (of order $3 \cdot 10^{-4}$ $M_\odot$ yr^{-1}) than those in the r^{-2} case ($\sim 2 \cdot 10^{-5}$ $M_\odot$ yr^{-1}). Tuning the outer dust radius to where the dust reaches 20 K implies an increase in the MLR by factors of ∼15 over the past 22–34 kyr for these two stars.

One interpretation of the lower temperature at the inner dust radius is that the MLR recently stopped and that the CSE now drifts outwards. Comparing the inner radius to that with dust temperatures of ∼950 K at the inner radius implies a flow timescale of 110–150 yr for these two stars. This is short compared to the typical post-AGB transition timescale of a few thousand years (Miller Bertolami 2016); thus, having three objects (TRM 74 as well) in our sample would be statistically unlikely.

Another possibility to explain the very poor fits is a deviation from spherical symmetry of the CSE and/or the role of binarity. Disk and spiral structures can manifest themselves in the SED, as shown by Wiegert et al. (2020) in one particular case.

Table 2. Highly red Galactic carbon stars.

Identifier	Period (days)	$V_{\rm exp}$ (km s^{-1})	Lum. (L$_\odot$)	D (kpc)	MLR$_{\rm DUSTY}$ (10^{-5}M$_\odot$ yr^{-1})	$V_{\rm exp,DUSTY}$ (km s^{-1})	GTD	MLR$_{\rm scaled}$ (10^{-5}M$_\odot$ yr^{-1})
AFGL 190	1060	18.0	16 400	3.30	5.7	10.5	67	3.3
AFGL 341	815	14.2	12 500	2.81	2.6	14.2	199	2.6
IRAS 03448+4432	729	13.3	11 100	2.31	1.4	20.6	477	2.2
AFGL 865	696	16.6	10 600	1.72	1.5	17.9	234	1.6
IRAS 08074−3615	832	21.7	12 700	2.95	2.0	19.2	156	1.7
AFGL 2494	783	20.5	12 000	1.50	1.4	20.0	191	1.3
AFGL 3068	696	15.1	10 600	1.05	3.9	13.9	168	3.6

Notes. Data from Table 4 in Gr16 where references are given. Columns 6 and 7 give the gas MLR and gas expansion velocity for a GTD ratio of 200 as outputted by DUSTY. Column 8 gives the GTD ratio that makes the modelled expansion velocity equal to the expansion velocity, and the last column lists the gas MLR for that GTD ratio.

That (sub)stellar companions can shape the molecular outflows is well established for MW AGB stars (see the review by Decin et al. 2020), but the current observations lack spatial resolution to study this. Companions can also change the shape of the low-J CO lines (Vermeulen et al. 2025); however, at the current signal-to-noise ratio as well as the given spectral and spatial resolutions, the profiles show the standard parabolic profile (see Fig. B.1 for IRAS 05315, and the supplementary material for IRAS 05495 and TRM 74).

6.4. MLR from simple CO scaling relation

The relation in Ramstedt et al. (2008) was used to determine the total MLR from the observed CO intensity:

$$\dot{M} = s_{\rm J} \left(A\,\theta^2\,D^2\right)^{a_{\rm J}} {\rm V}_{\rm exp}^{b_{\rm J}}\, f_{\rm CO}^{c_{\rm J}} \quad (3)$$

with $s_{\rm J} = (1.3 \pm 0.7) \cdot 10^{-11}$ M$_\odot$ yr^{-1}, $a_{\rm J} = 0.82$, $b_{\rm J} = 0.46$, and $c_{\rm J} = -0.59$ for the J= 2–1 transition. The distance, D, was set to 50 kpc for the LMC and 60 kpc for the SMC, and the averaged beam size (θ) was taken as the geometric average of the values in Table E.1. The integrated intensity, A, in this formula is expressed units of Kelvin km s^{-1}. The values in Table E.1 are in Jansky km s^{-1} and are converted.

The unknown in the equation is the abundance ratio of CO relative to H_2. In Gr16 a value of $f_{\rm CO/H_2}$ of $4.5 \cdot 10^{-4}$ was used for the LMC. New calculations (Marigo & Groenewegen, unpublished) confirm that, when the object becomes a C star, the CO abundance is nearly constant over the remainder of the AGB evolution. For a star with an initial mass of 2 M$_\odot$, this value is 10.8, 6.0, and $3.0 \cdot 10^{-4}$ for initial abundances of Z= 0.014, 0.008, and 0.004, respectively. The change over the C-star's lifetime is only about $0.1 \cdot 10^{-4}$. Therefore, 3.0 and $6.0 \cdot 10^{-4}$ were adopted for $f_{\rm CO}$ in the SMC and LMC, respectively. The resulting MLR estimates are listed in the Column 14 of Table E.2.

Errors in the MLR estimate were calculated based on the error in the leading coefficient, $s_{\rm J}$, the error in the observed intensity, the error in the expansion velocity, and an error of $1 \cdot 10^{-4}$ in $f_{\rm CO}$. The error in $s_{\rm J}$ dominates, and the total relative error is quite uniform within 54 and 59%. The error in the CO-based MLR is large, but this is inherent when using only a single CO line and a simple fitting formula.

Figure 3 compares dust-based and CO-based MLRs. The errors in the CO-based MLR dominate the plot, and there is very large scatter. A straight average of the 26 objects with CO detections and reliable RT models indicates that the dust-based MLRs are, on average, a factor 1.6 larger than the CO-based ones, and a factor of 0.8 in the median. The difference between the mean and the median also indicates large scatter. Additional CO data in other transitions combined with proper modelling of the CO lines is required to further investigate this possible discrepancy.

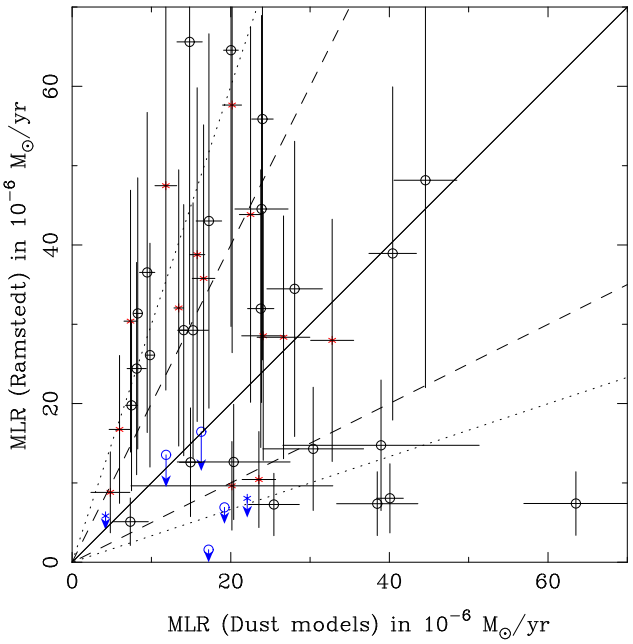

Fig. 3. Comparison of the MLRs from dust RT fitting and CO (2–1) line emission. The solid line shows the one-to-one correspondence between these MLRs, and the dashed (dotted) lines indicate factors of 2 (3) difference in the MLRs. Upper limits on the gas MLR derived from CO non-detections are marked in blue. The red stars indicate unreliable models (see details in Appendix D).

7. Discussion

Figure 4 compares the results for the LMC and SMC to observations of Galactic objects (cf. Figure 2 in Gr16). The Galactic sample was compiled from Schöier & Olofsson (2001), Ramstedt & Olofsson (2014), and Danilovich et al. (2015). As in Gr16, seven of the reddest known Galactic C stars, partly with SiC in absorption, were added (see Table 2; data were taken from Table 4 in Gr16). Apart from redness, these stars were selected to have a pulsation period in order to derive a

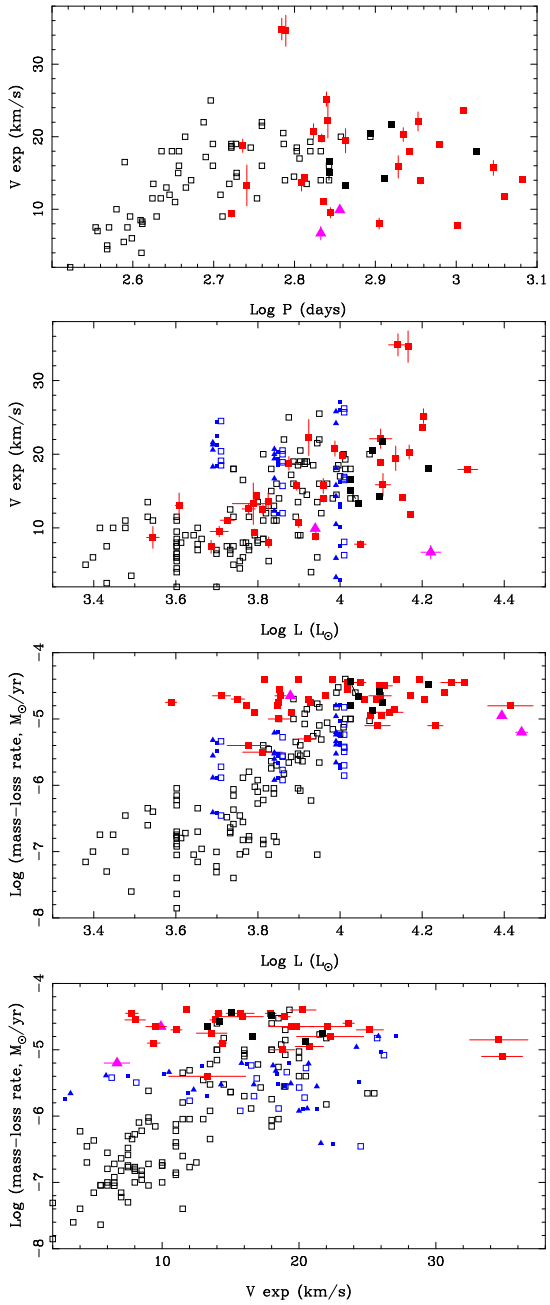

Fig. 4. From top to bottom: $V_{\rm exp}$ plotted against pulsation period and luminosity, $\dot{M}$ (the geometric mean from Columns 11–13 in Table E.2) plotted against luminosity and $V_{\rm exp}$. Plotted are the C stars in the LMC (red-filled squares) and in the SMC (pink-filled triangles), Galactic C stars from Schöier & Olofsson (2001), Ramstedt & Olofsson (2014), and Danilovich et al. (2015) (open black squares), and the highly red Galactic C stars (black-filled squares). Objects with very large error bars in the expansion velocity (>2.4 km s^{-1} in the SMC, >3.0 km s^{-1} in the LMC) are not plotted. The blue symbols represent models selected from Bladh et al. (2019) (see text) and indicate the SMC (blue-filled triangles), LMC (blue-filled squares), and MW (open blue squares). The SMC and MW sources are offset by −0.01 and +0.01 dex in log L for clarity.

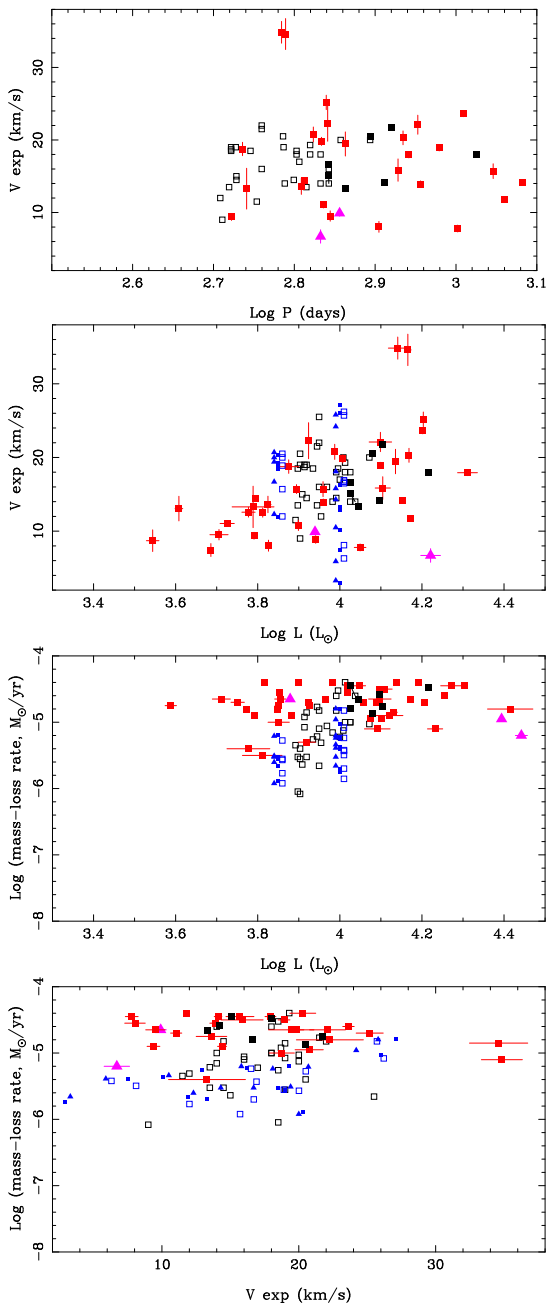

Fig. 5. As Figure 4, but with the pulsation period limited to > 500 days.

luminosity from the *PL*-relation in Groenewegen & Whitelock (1996) so that a distance could be estimated. This unfiltered comparison reveals very little overlap between the Galactic and MC sample in most of the parameters. It is clear that the MC samples longer periods (and higher luminosities). Figure 5 shows the same plots but where the Galactic sample was limited to stars with a period longer than 500 days (log P > 2.7). This is about the shortest period in the MC sample (see Table E.2). The overlap in properties has improved. From the $V_{\rm exp}$ – log P diagram we find no difference between the LMC and MW, although the two SMC sources appear to exhibit a lower expansion velocity at that period. Comparing this and Fig. 4, it is striking to see that, in the LMC, our CO observations sample a population of intermediate luminosities (log L ∼ 3.6–3.85, L ∼ 4000–7000 L$_\odot$) with large MLRs that have no counterpart in the Galactic sample considered here. As a C star in the LMC has greater carbon excess than a MW C star at the same luminosity (due to lower oxygen to overcome in the LMC) its MLR may well be higher.

The comparison of MW and MC samples remains problematic, and this complicates quantifying with certainty any metallicity dependence of MLRs, GTD ratios, and $V_{\rm exp}$. The

Nearby Evolved Stars Survey (NESS; Scicluna et al. 2022) aims to construct a volume-complete sample of MW AGB stars. Their samples are divided into several tiers based on the DPR and out to a limiting distance, which differs per tier. AFGL 865, 2494, and 3068 are present in the latest version of the catalogue (McDonald et al. 2025)[6], specifically in the 'high' tier. This tier indicates $3 \cdot 10^{-9} <$ DPR $< 1 \cdot 10^{-7}$ $M_\odot\,yr^{-1}$and a limiting distance of 1.2 kpc. Indeed, these three stars are closest to the Sun according to our distance estimates, although two lie beyond 1.2 kpc. The distances in McDonald et al. (2025) have been updated for individual objects compared to Scicluna et al. (2022), and the stars in the 'high' and 'extreme' tiers now extend to several kiloparsecs. In addition, our DPR for AFGL 3068 would place it in the 'extreme' tier. Considering this, the four stars in Table 2 should also have been included in NESS, but they were not. This simply illustrates how difficult it is to create volume-complete samples given the uncertainties in distances (and, thus, luminosities and MLRs) for MW AGB stars. An additional complication in comparing samples comes from the fact that stars with high DPRs are rare. Using the number of stars per tier from McDonald et al. (2025) and excluding 5% of stars with the largest outlying distance per tier, assuming a volume density proportional to the square of the distance[7] one can estimate that the 'high' tier represents about 1% of all AGB stars, while the 'extreme' tier is 20 times less abundant.

8. Summary and conclusions

Our observations present the first detection of CO in SMC AGB stars (in two out of three targets) and extend the detections in LMC AGB carbon stars from 4 to 37. We reported the first detection of ^{13}CO for a LMC carbon star, IRAS 05568.

Radiation-driven wind theory predicts $V_{\rm exp}$ ~GTD$^{-0.5}$ (e.g. Habing et al. 1994). The median GTD is derived to be 1500 for the three SMC stars, 400 for the 42 LMC stars, and 190 for the seven Galactic stars. Between SMC and LMC, one would therefore expect a difference in expansion velocities by a factor of 1.9. The two stars detected in the SMC have among the lowest expansion velocities – 6.7 km s^{-1} and 9.9 km s^{-1}– while the median among the LMC detections is 15.7 km s^{-1}. This is indeed close to a factor of two, but only based on a very small sample. The difference in the GTD ratio between LMC and the MW implies a difference in expansion velocity by a factor of about 1.4, which is not supported by the present data. Interestingly, a few LMC objects have expansion velocities above 30 km s^{-1} (31–35 km s^{-1}). No counterparts exist in the Galactic samples studied here, although such carbon stars do exist. For example, 13 sources among the 331 C stars detected in CO in Groenewegen et al. (2002b) have expansion velocities ranging from 31 to 43 km s^{-1}.

Extending the sample further to better probe the range of intermediate luminosities at slightly lower MLRs is a possibility. This ALMA programme has demonstrated that CO line intensities can be predicted sufficiently accurately to ensure a high detection rate. Such a programme would require an order of magnitude more observing time (approximately 100 hours) for a dozen objects. One approach we want to pursue in the future is to obtain observations at other transitions of selected stars and model the line shapes and intensities with a RT code. This would constrain the CO emission region (and the role of photodissociation) and lead to a more accurate estimate of the gas MLR.

[6] The file table-g6.tsv from the supplementary-tables directory as retrieved from the MNRAS website.

[7] As the limiting distances are greater than the typical scale height of AGB stars of 100 pc.

Data availability

The complete set of figures shown in Appendices A, B, C, and D is available at https://doi.org/10.5281/zenodo.21700114.

Acknowledgements. This paper makes use of the following ALMA data: ADS/JAO.ALMA#2023.1.00681.S. ALMA is a partnership of ESO (representing its member states), NSF (USA) and NINS (Japan), together with NRC (Canada) and NSC and ASIAA (Taiwan) and KASI (Republic of Korea), in cooperation with the Republic of Chile. The Joint ALMA Observatory is operated by ESO, AUI/NRAO and NAOJ. M.G. acknowledges assistance from Allegro, the ALMA Regional Centre node in the Netherlands, and in particular Megan Lewis. AN acknowledges support from the Narodowe Centrum Nauki (NCN), Poland, through the SONATA BIS grant UMO-2020/38/E/ST9/00077. R.S.'s contribution to the research described here was carried out at the Jet Propulsion Laboratory, California Institute of Technology, under a contract with NASA (80NM0018D0004), and funded in part by NASA via ADAP awards. L. Decin acknowledge support from the FWO grant G0B3823N, the FWO grant G099720N, the KU Leuven C1 excellence grant MAESTRO C16/17/007, and the KU Leuven Methusalem SOUL grant METH/24/012. K.J. acknowledges the support of Swedish National Space Agency.

References

Abia, C., & Isern, J. 2000, ApJ, 536, 438
Aringer, B., Girardi, L., Nowotny, W., Marigo, P., & Lederer, M. T. 2009, A&A, 503, 913
Beichmann, C. A. 1985, Infrared Astronomical Satellite (IRAS) catalogs and atlases. Explanatory supplement
Bladh, S., Eriksson, K., Marigo, P., Liljegren, S., & Aringer, B. 2019, A&A, 623, A119
Boyer, M. L., Srinivasan, S., van Loon, J. T., et al. 2011, AJ, 142, 103
Cardelli, J. A., Clayton, G. C., & Mathis, J. S. 1989, ApJ, 345, 245
Cioni, M.-R. L., Clementini, G., Girardi, L., et al. 2011, A&A, 527, A116
Cutri, R. M., & et al. 2014, VizieR Online Data Catalog, 2328, 0
Cutri, R. M., Skrutskie, M. F., van Dyk, S., et al. 2012, VizieR Online Data Catalog, II/281
Danilovich, T., Teyssier, D., Justtanont, K., et al. 2015, A&A, 581, A60
De Beck, E., Decin, L., de Koter, A., et al. 2010, A&A, 523, A18
Decin, L., Montargès, M., Richards, A. M. S., et al. 2020, Science, 369, 1497
Egan, M. P., Price, S. D., Kraemer, K. E., et al. 2003, VizieR Online Data Catalog, V/114
Engels, D., & Bunzel, F. 2015, A&A, 582, A68
Eriksson, K., Nowotny, W., Höfner, S., Aringer, B., & Wachter, A. 2014, A&A, 566, A95
Gaia Collaboration (Vallenari, A., et al.) 2023, A&A, 674, A1
Goldman, S. R., van Loon, J. T., Zijlstra, A. A., et al. 2017, MNRAS, 465, 403
Goldman, S. R., van Loon, J. T., Gómez, J. F., et al. 2018, MNRAS, 473, 3835
Groenewegen, M. A. T. 2004, A&A, 425, 595
Groenewegen, M. A. T. 2012, A&A, 543, A36
Groenewegen, M. A. T. 2022, A&A, 659, A145
Groenewegen, M. A. T., & Whitelock, P. A. 1996, MNRAS, 281, 1347
Groenewegen, M. A. T., & Sloan, G. C. 2018, A&A, 609, A114
Groenewegen, M. A. T., Oudmaijer, R. D., & Ludwig, H. G. 1997, MNRAS, 292, 686
Groenewegen, M. A. T., Sevenster, M., Spoon, H. W. W., & Pérez, I. 2002a, A&A, 390, 501
Groenewegen, M. A. T., Sevenster, M., Spoon, H. W. W., & Pérez, I. 2002b, A&A, 390, 511
Groenewegen, M. A. T., Vlemmings, W. H. T., Marigo, P., et al. 2016, A&A, 596, A50
Groenewegen, M. A. T., Nanni, A., Cioni, M. R. L., et al. 2020, A&A, 636, A48
Gruendl, R. A., Chu, Y. H., Seale, J. P., et al. 2008, ApJ, 688, L9
Habing, H. J., Tignon, J., & Tielens, A. G. G. 1994, A&A, 286, 523
Hofmeister, A. M., Keppel, E., & Speck, A. 2003, MNRAS, 345, 16
Höfner, S., & Olofsson, H. 2018, A&A Rev., 26, 1
Ishihara, D., Onaka, T., Kataza, H., et al. 2010, A&A, 514, A1
Ita, Y., Onaka, T., Tanabé, T., et al. 2010, PASJ, 62, 273

Ivezić, Ž., Nenkova, M., & Elitzur, M. 1999, DUSTY: Radiation transport in a dusty environment, Astrophysics Source Code Library
Jäger, C., Mutschke, H., & Henning, T. 1998, A&A, 332, 291
Kato, D., Nagashima, C., Nagayama, T., et al. 2007, PASJ, 59, 615
Kato, D., Ita, Y., Onaka, T., et al. 2012, AJ, 144, 179
Kemper, F., Stark, R., Justtanont, K., et al. 2003, A&A, 407, 609
Kerschbaum, F., & Olofsson, H. 1999, A&AS, 138, 299
Lagadec, E., Zijlstra, A. A., Mauron, N., et al. 2010, MNRAS, 403, 1331
Lebzelter, T., Mowlavi, N., Marigo, P., et al. 2018, A&A, 616, L13
Leksina, I., & Penkina, N. 1967, Fizik. Metall. Metalloved., 23, 344
Lenz, P., & Breger, M. 2005, Commun. Asteroseismol., 146, 53
Mainzer, A., Bauer, J., Grav, T., et al. 2011, ApJ, 731, 53
Mainzer, A., Bauer, J., Cutri, R. M., et al. 2014, ApJ, 792, 30
Mattsson, L., Wahlin, R., & Höfner, S. 2010, A&A, 509, A14
McDonald, I., Boyer, M. L., Groenewegen, M. A. T., et al. 2019, MNRAS, 484, L85
McDonald, I., Uttenthaler, S., Zijlstra, A. A., Richards, A. M. S., & Lagadec, E. 2020, MNRAS, 491, 1174
McDonald, I., Srinivasan, S., Scicluna, P., et al. 2025, MNRAS, 541, 516
McMullin, J. P., Waters, B., Schiebel, D., Young, W., & Golap, K. 2007, in Astronomical Society of the Pacific Conference Series, 376, Astronomical Data Analysis Software and Systems XVI, eds. R. A. Shaw, F. Hill, & D. J. Bell, 127
Miller Bertolami, M. M. 2016, A&A, 588, A25
Min, M., Hovenier, J. W., & de Koter, A. 2005, A&A, 432, 909
Morgan, D. H., Cannon, R. D., Hatzidimitriou, D., & Croke, B. F. W. 2003, MNRAS, 341, 534
Moshir, M., Copan, G., Conrow, T., et al. 1993, VizieR Online Data Catalog: IRAS Faint Source Catalog, |b| > 10, Version 2.0
Nanni, A. 2019, MNRAS, 482, 4726
Nanni, A., Bressan, A., Marigo, P., & Girardi, L. 2013, MNRAS, 434, 2390
Nanni, A., Bressan, A., Marigo, P., & Girardi, L. 2014, MNRAS, 438, 2328
Nanni, A., Marigo, P., Groenewegen, M. A. T., et al. 2016, MNRAS, 462, 1215
Nanni, A., Marigo, P., Girardi, L., et al. 2018, MNRAS, 473, 5492
Nanni, A., Groenewegen, M. A. T., Aringer, B., et al. 2019, MNRAS, 487, 502
Olofsson, H., González Delgado, D., Kerschbaum, F., & Schöier, F. L. 2002, A&A, 391, 1053
Pégourié, B. 1988, A&A, 194, 335
Pitman, K. M., Hofmeister, A. M., Corman, A. B., & Speck, A. K. 2008, A&A, 483, 661
Press, W. H., Teukolsky, S. A., Vetterling, W. T., & Flannery, B. P. 1992, Numerical recipes in FORTRAN
Ramstedt, S., & Olofsson, H. 2014, A&A, 566, A145
Ramstedt, S., Schöier, F. L., Olofsson, H., & Lundgren, A. A. 2008, A&A, 487, 645
Ramstedt, S., Vlemmings, W. H. T., Doan, L., et al. 2020, A&A, 640, A133
Saberi, M., Vlemmings, W. H. T., & De Beck, E. 2019, A&A, 625, A81
Schöier, F. L., & Olofsson, H. 2001, A&A, 368, 969
Scicluna, P., Kemper, F., McDonald, I., et al. 2022, MNRAS, 512, 1091
Seale, J. P., Meixner, M., Sewiło, M., et al. 2014, AJ, 148, 124
Skowron, D. M., Skowron, J., Udalski, A., et al. 2021, ApJS, 252, 23
Soszyński, I., Udalski, A., Szymański, M. K., et al. 2009, Acta Astron., 59, 239
Soszyński, I., Udalski, A., Szymański, M. K., et al. 2011, Acta Astron., 61, 217
Tanabé, T., Kučinskas, A., Nakada, Y., Onaka, T., & Sauvage, M. 2004, ApJS, 155, 401
Uchiyama, M., & Ichikawa, K. 2019, ApJ, 883, 6
Ventura, P., Dell'Agli, F., Lugaro, M., et al. 2020, A&A, 641, A103
Ventura, P., Dell'Agli, F., Romano, D., et al. 2021, A&A, 655, A6
Vermeulen, O., Esseldeurs, M., Malfait, J., et al. 2025, A&A, 700, A85
Wallström, S. H. J., Scicluna, P., Srinivasan, S., et al. 2025, A&A, 704, A276
Whitney, B. A., Sewilo, M., Indebetouw, R., et al. 2008, AJ, 136, 18
Wiegert, J., Groenewegen, M. A. T., Jorissen, A., Decin, L., & Danilovich, T. 2020, A&A, 642, A142
Wood, P. R., Whiteoak, J. B., Hughes, S. M. G., et al. 1992, ApJ, 397, 552
Woods, P. M., Schöier, F. L., Nyman, L.-Å., & Olofsson, H. 2003, A&A, 402, 617
Wright, E. L., Eisenhardt, P. R. M., Mainzer, A. K., et al. 2010, AJ, 140, 1868
Zubko, V. G., Mennella, V., Colangeli, L., & Bussoletti, E. 1996, MNRAS, 282, 1321

Appendix A: Image cut-outs

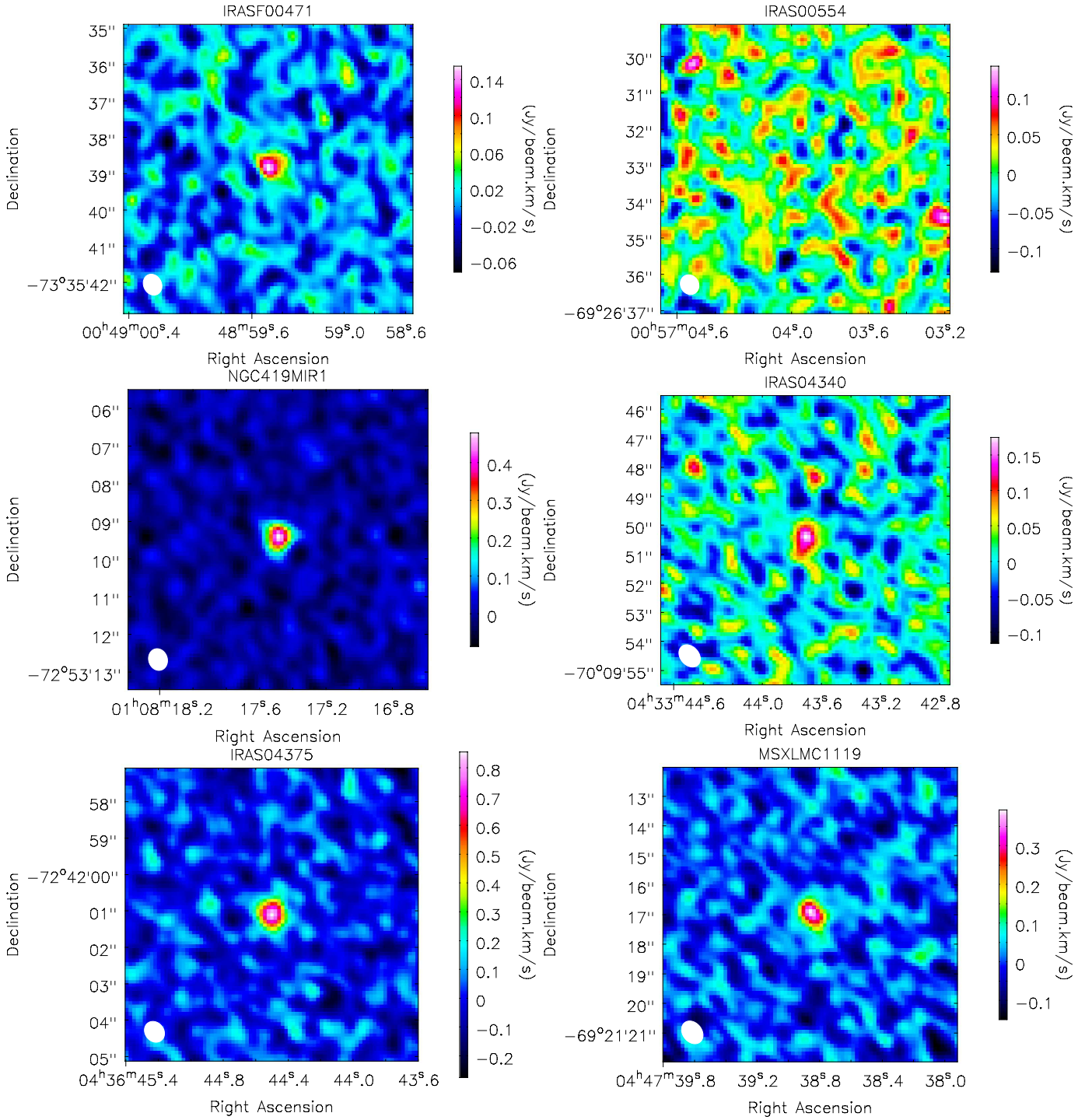

Fig. A.1: Example of 10″×10″ zero-moment maps of the ^{12}CO emission centred on the source. The white ellipse in the lower left corners represents the beam. The complete set of figures is available via Zenodo.

Appendix B: CO line profiles

Figure B.1 shows the ^{12}CO(2–1) and ^{13}CO(2–1) line profiles. The blue lines refer to the best fitting models. In case of a ^{13}CO non-detection a model representing the 3σ upper limit on the integrated intensity is shown, plotted at the systemic velocity of the ^{12}CO emission and for a fixed expansion velocity. In case of a ^{12}CO non-detection a model representing the 3σ upper limit on the integrated intensity is shown for a random systemic velocity and a fixed expansion velocity of 15 km s^{-1} (9 km s^{-1} for the SMC source). The complete set of figures is available via Zenodo.

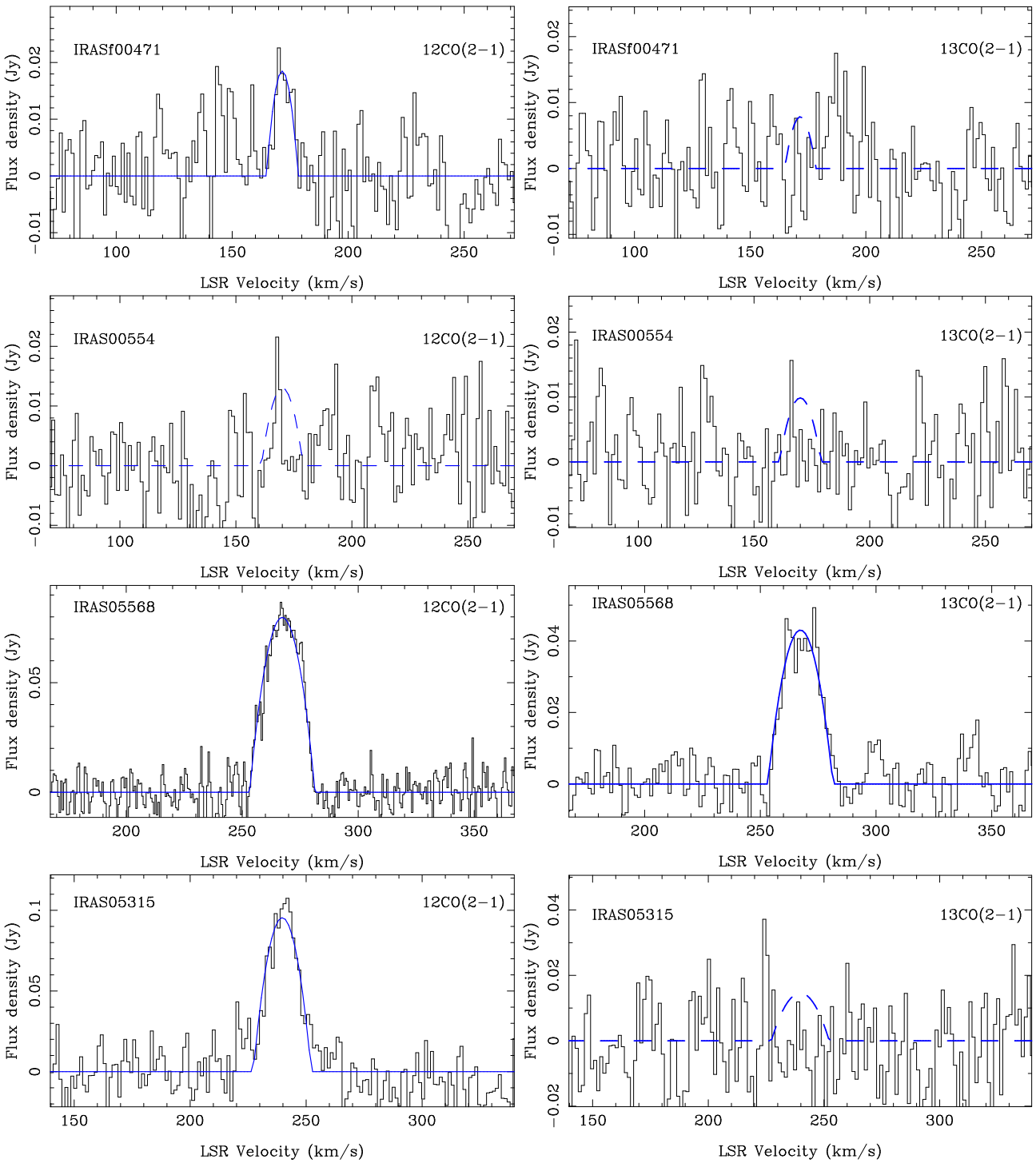

Fig. B.1: Examples of ^{12}CO(2–1) and ^{13}CO(2–1) line profiles. The best fitting models are shown as blue full lines, and the 3σ upper limits in the case of non-detections (see text) are shown as dashed lines. The complete set of figures is available via Zenodo

Appendix C: Period analysis

Tables C.1 and C.2 list the derived periods based on VMC and WISE data, respectively. Figures C.1 and C.2 show examples of the LCs and the fitted models.

Table C.1: Period analysis in the K-band.

Name	Ra_i (deg)	Dec_i (deg)	Ra_f (deg)	Dec_f (deg)	Dist ($''$)	N	P_K (d)	σ_{P_K} (d)	AmpK (mag)	σ_{AmpK} (mag)	K (mag)	σ_K (mag)	χ^2_K
IRASf00471	12.247879	-73.594121	12.247876	-73.594104	0.06	16	623.6	27.1	0.47	0.10	11.184	0.052	244.2
IRAS00554	14.266367	-73.587387	14.266429	-73.587419	0.13	15	898.8	84.8	0.71	0.15	11.493	0.065	207.8
NGC419MIR1	17.072829	-72.885948	17.072880	-72.885959	0.06	7	691.2	22.7	0.83	0.16	14.331	0.056	53.9
IRAS04340	68.432358	-70.164048	68.431999	-70.164004	0.47	15	435.7	16.0	0.30	0.07	11.183	0.036	109.9
IRAS04375	69.185429	-72.700292	69.185315	-72.700325	0.17	15	746.5	78.8	0.66	0.10	12.192	0.022	48.9
MSXLMC1119	71.911867	-69.354717	71.911847	-69.354718	0.03	16	488.5	5.3	0.49	0.03	11.571	0.016	32.9
IRAS04496	72.326917	-69.887359	72.327053	-69.887356	0.17	12					10.983	0.022	43.9
IRAS04523	72.962163	-70.642241	72.962073	-70.642208	0.16	18	857.4	42.9	0.45	0.07	11.365	0.083	204.7
SAGEMCJ045344	73.434475	-66.196132	73.434395	-66.196116	0.13	15	762.9	47.9	0.89	0.16	15.520	0.030	9.4
IRAS04557	73.912421	-67.819591	73.912385	-67.819623	0.12	15	651.3	2.9	0.69	0.01	12.839	0.004	1.1
MSXLMC1220	73.924079	-68.956284	73.924134	-68.956312	0.12	14	433.9	31.5	0.42	0.12	11.337	0.105	456.7
MSXLMC1303	74.675175	-68.120835	74.675133	-68.120909	0.27	16	1184.2	852.1	0.28	0.21	15.765	0.194	375.3
MSXLMC1282	75.253751	-67.589911	75.253617	-67.589880	0.21	16	498.4	27.5	0.43	0.09	11.379	0.063	461.2
ERO0502315	75.631267	-68.093301	75.631594	-68.093646	1.32	1							
MSXLMC91	75.910721	-68.886864	75.910566	-68.886888	0.22	14	889.4	13.9	0.80	0.03	13.002	0.014	17.7
TRM74	75.929217	-66.749036	75.929193	-66.749080	0.17	4							
ERO0504056	76.023421	-68.394531	76.024634	-68.394107	2.22	10					19.168	0.061	0.5
MSXLMC87	77.581901	-69.830974	77.581756	-69.830970	0.18	14	613.8	789.8	0.23	0.52	11.078	0.440	119.9
IRAS05113	77.736892	-69.591809	77.736634	-69.591819	0.33	14	756.7	1029.5	0.36	0.35	11.173	0.296	845.7
IRAS05132	78.212758	-69.630653	78.212652	-69.630661	0.14	14	697.6	11.3	0.65	0.01	12.433	0.006	1.1
IRAS05133	78.257442	-69.564153	78.257558	-69.564206	0.24	14					16.239	0.006	0.2
ERO0518484	79.701683	-69.559625	79.701263	-69.559886	1.08	30					16.648	0.010	3.2
IRAS05190	79.734463	-67.751243	79.734423	-67.751236	0.06	14	894.1	23.7	0.98	0.02	13.848	0.016	14.2
TRM88	80.080875	-66.596626	80.080755	-66.596613	0.18	16					10.704	0.034	169.4
MSXLMC527	80.581604	-65.722303	80.582272	-65.721907	1.74	16	1068.9	221.1	0.37	0.09	13.600	0.076	205.9
ERO0525406	81.419396	-70.140901	81.419323	-70.141075	0.63	15					17.126	0.010	0.6
MSXLMC474	81.466101	-68.776167	81.466071	-68.776204	0.14	15	640.7	62.4	0.72	0.09	11.635	0.034	60.3
IRAS05315	82.683892	-71.716808	82.683878	-71.716831	0.08	29					17.029	0.014	4.7
MSXLMC1780	83.257483	-68.399565	83.257376	-68.399582	0.15	17	827.2	6.2	1.00	0.04	13.452	0.022	20.2
IRAS05373	84.100671	-72.692391	84.100610	-72.692374	0.08	15	812.9	37.8	0.63	0.11	12.659	0.080	178.2
MSXLMC971	84.966001	-70.021426	84.965917	-70.021386	0.18	14	619.9	24.8	0.96	0.02	13.503	0.018	4.3
MSXLMC937	85.150438	-69.880528	85.150268	-69.880480	0.27	14	642.5	93.2	0.70	0.04	11.358	0.054	26.0
IRAS05416	85.336488	-69.078812	85.336413	-69.078815	0.11	15	892.8	20.8	0.92	0.28	17.726	0.055	0.3
LMCLPV76711	85.571808	-70.538971	85.571700	-70.539003	0.18	17	515.6	23.7	0.36	0.11	11.918	0.039	160.2
IRAS05495	87.250017	-70.556247	87.250043	-70.556172	0.27	12					19.167	0.059	0.2
ERO0550261	87.608879	-69.934185	87.609920	-69.934187	1.29	8					19.254	0.074	0.5
IRAS05515	87.708112	-71.393213	87.708039	-71.393240	0.13	15	643.9	10.5	0.59	0.04	13.212	0.016	23.9
MSXLMC1797	87.889933	-71.326194	87.887844	-71.325661	3.08	1							
IRAS05568	89.161538	-67.892749	89.161484	-67.892776	0.13	11	1118.7	4.7	1.48	0.04	17.458	0.025	0.4
IRAS06028	90.688067	-67.378653	90.688066	-67.378676	0.08	14	871.2	9.5	1.00	0.05	13.454	0.016	25.3
IRAS06108	92.544704	-70.767581	92.544461	-70.767573	0.29	26	530.8	2.1	0.70	0.03	12.954	0.009	13.5
IRAS05506	87.485502	-70.886597	87.485612	-70.886609	0.14	15	1310.5	64.4	0.93	0.04	12.429	0.046	5.5
IRAS05125	78.003364	-70.540098	78.003223	-70.540034	0.29	16	1347.9	44.1	0.46	0.02	15.289	0.013	11.8
ERO0529379	82.407854	-72.831365	82.406845	-72.831189	2.10	30					16.806	0.056	102.2
ERO0518117	79.548769	-70.507508	79.549041	-70.507507	0.33	5					18.975	0.079	0.8

Notes. Listed are the source name, the input coordinates used to search the VMC archive, the "final" coordinates being the average of the coordinates of all entries contributing to the LC, the distance between input and final coordinates, the number of data points, period, amplitude, and mean magnitude (with errors), and the reduced χ^2. All error bars have been scaled to give a reduced χ^2 of unity.

Table C.2: Period analysis in the WISE bands.

Name	Ra_i (deg)	Dec_i (deg)	Ra_f (deg)	Dec_f (deg)	Dist ($''$)	$P1$ (d)	σ_{P1} (d)	$P2$ (d)	σ_{P2} (d)	Amp1 (mag)	σ_{A1} (mag)	$W1$ (mag)	σ_{W1} (mag)	$\chi^2_{r,W1}$	Amp2 (mag)	σ_{A2} (mag)	$W2$ (mag)	σ_{W2} (mag)	$\chi^2_{r,W2}$
IRASf00471	12.247879	-73.594120	12.247892	-73.594114	0.07	680	1.0	680	0.8	0.57	0.01	8.956	0.004	26.4	0.52	0.01	7.777	0.003	22.4
IRAS00554	14.266367	-73.587387	14.266423	-73.587432	0.18	898	1.1	890	0.9	0.63	0.02	9.133	0.004	33.9	0.59	0.01	7.675	0.004	32.1
NGC419MIR1	17.072829	-72.885948	17.073007	-72.885810	0.53	717	1.3	718	0.6	0.40	0.02	9.881	0.012	32.7	0.53	0.01	8.723	0.007	13.6
IRAS04340	68.432358	-70.164048	68.432030	-70.164015	0.42	439	0.5	440	0.4	0.51	0.02	9.740	0.005	62.0	0.46	0.01	8.701	0.004	42.2
IRAS04375	69.185429	-72.700292	69.185376	-72.700302	0.11	692	0.6	695	0.5	0.60	0.01	9.719	0.004	27.2	0.52	0.01	8.091	0.003	22.0
MSXLMC1119	71.911867	-69.354717	71.911858	-69.354727	0.09	545	0.3	544	0.3	0.47	0.01	9.468	0.002	11.2	0.44	0.01	8.227	0.002	12.6
IRAS04496	72.326917	-69.887359	72.327036	-69.887369	0.16	824	3.7	816	4.6	0.12	0.01	8.029	0.004	23.7	0.10	0.01	7.027	0.004	35.0
IRAS04523	72.962163	-70.642240	72.962078	-70.642242	0.13	875	0.8	874	0.6	0.70	0.01	8.940	0.003	28.8	0.64	0.01	7.428	0.003	21.4
SAGEMCJ045344	73.434475	-66.196132	73.434463	-66.196115	0.13	761	0.5	761	0.4	0.78	0.01	11.168	0.003	20.7	0.70	0.01	8.844	0.002	18.4
IRAS04557	73.912421	-67.819591	73.912433	-67.819599	0.11	728	0.6	732	0.4	0.70	0.01	10.078	0.003	32.9	0.59	0.01	8.266	0.002	19.7
MSXLMC1220	73.924079	-68.956284	73.924132	-68.956273	0.11	513	0.5	514	0.3	0.40	0.01	9.264	0.004	45.0	0.33	0.01	8.062	0.002	20.7
MSXLMC1303	74.675175	-68.120835	74.675107	-68.120882	0.23	1005	4.5	1005	4.4	0.49	0.03	11.086	0.011	329.9	0.42	0.03	8.575	0.009	359.5
MSXLMC1282	75.253750	-67.589910	75.253733	-67.589893	0.10	608	0.7	609	0.7	0.53	0.01	8.930	0.004	62.7	0.42	0.02	7.629	0.004	77.0
ERO0502315	75.631267	-68.093300	75.631233	-68.093309	0.37			15938	449.4			15.753	0.025	1.9	0.80	0.03	12.547	0.032	3.7
MSXLMC91	75.910721	-68.886864	75.910640	-68.886878	0.15	897	0.8	897	0.7	0.77	0.02	9.624	0.003	30.5	0.66	0.01	7.740	0.002	26.7
TRM74	75.929217	-66.749036	75.929257	-66.749079	0.32	8092	3137	10256	1631	0.04	0.02	15.031	0.018	2.2	0.05	0.01	12.513	0.010	2.3
ERO0504056	76.023421	-68.394531	76.023374	-68.394518	0.44			8920	277.1						0.29	0.01	13.329	0.006	2.0
MSXLMC87	77.581900	-69.830974	77.581757	-69.830969	0.18	617	1.7	614	1.6	0.37	0.03	8.870	0.008	251.9	0.34	0.01	7.662	0.007	255.9
IRAS05113	77.736892	-69.591809	77.736743	-69.591808	0.21	633	1.1	629	0.9	0.65	0.03	9.156	0.006	123.3	0.52	0.02	7.735	0.004	73.9
IRAS05132	78.212758	-69.630653	78.212667	-69.630640	0.15	683	0.7	681	0.5	0.63	0.01	9.452	0.003	38.8	0.58	0.01	7.928	0.002	22.9
IRAS05133	78.257442	-69.564153	78.257370	-69.564149	0.51			702	6.8			16.282	0.209	0.0	0.08	0.02	13.869	0.007	1.7
ERO0518484	79.701683	-69.559625	79.701599	-69.559559	0.26			803	22.3			15.307	0.070	0.3	0.21	0.03	12.719	0.031	5.0
IRAS05190	79.734463	-67.751243	79.734384	-67.751229	0.15	960	1.6	950	1.1	0.96	0.02	10.293	0.006	154.4	0.77	0.01	8.081	0.004	106.9
TRM88	80.080875	-66.596626	80.080814	-66.596624	0.12	538	0.7	536	0.5	0.41	0.01	8.985	0.005	118.3	0.38	0.01	7.950	0.003	76.7
MSXLMC527	80.581604	-65.722303	80.582113	-65.722210	0.77							11.300	0.212	591.2			9.294	0.192	813.8
ERO0525406	81.419396	-70.140901	81.419409	-70.140876	0.09			828	27.8			15.703	0.351	4.4	0.26	0.13	13.297	0.087	3.1
MSXLMC474	81.466100	-68.776167	81.466072	-68.776173	0.10	617	0.8	625	0.5	0.55	0.02	9.098	0.004	83.5	0.51	0.01	7.653	0.002	41.0
IRAS05315	82.683892	-71.716808	82.684316	-71.716749	0.54	3111	199.8	2985	54.4	0.02	0.01	13.831	0.003	2.5	0.04	0.01	11.980	0.002	2.3
MSXLMC1780	83.257483	-68.399565	83.257332	-68.399570	0.22	848	0.8	848	0.7	0.76	0.01	10.304	0.003	67.9	0.69	0.01	8.240	0.003	68.3
IRAS05373	84.100671	-72.692390	84.100596	-72.692388	0.10	645	0.8	643	0.6	0.54	0.01	9.736	0.004	44.1	0.50	0.01	8.162	0.003	31.5
MSXLMC971	84.966000	-70.021426	84.966000	-70.021417	0.12	648	0.5	649	0.4	0.69	0.01	10.290	0.003	35.4	0.57	0.01	8.406	0.002	26.4
MSXLMC937	85.150438	-69.880528	85.150349	-69.880501	0.19	691	0.8	691	0.8	0.62	0.01	8.890	0.003	67.3	0.58	0.01	7.478	0.003	67.9
IRAS05416	85.336488	-69.078812	85.336451	-69.078794	0.18	901	0.9	907	0.9	1.07	0.01	12.479	0.004	48.8	0.92	0.01	9.451	0.003	97.7
LMCLPV76711	85.571808	-70.538970	85.571729	-70.539004	0.17	552	0.5	550	0.4	0.49	0.02	9.274	0.003	21.7	0.43	0.01	8.024	0.002	16.4
IRAS05495	87.250017	-70.556247	87.249892	-70.556277	0.43	11450	3220	6306	1753	0.05	0.02	15.472	0.010	2.2	0.03	0.02	13.434	0.010	2.3
ERO0550261	87.608879	-69.934185	87.608836	-69.934213	0.31	1100	2.5	1115	1.3	0.60	0.02	15.518	0.010	3.2	0.69	0.01	11.527	0.004	32.3
IRAS05515	87.708112	-71.393213	87.708059	-71.393231	0.13	664	0.6	667	0.4	0.62	0.01	10.281	0.004	45.8	0.54	0.01	8.504	0.002	28.9
MSXLMC1797	87.889933	-71.326194	87.889961	-71.326161	0.17	686	2.2	704	1.4	0.74	0.03	15.589	0.017	9.0	0.42	0.02	11.548	0.007	74.7
IRAS05568	89.161538	-67.892749	89.161467	-67.892763	0.18	1206	1.0	1211	0.9	1.27	0.01	12.090	0.003	65.0	1.06	0.01	9.069	0.002	100.9
IRAS06028	90.688067	-67.378653	90.688041	-67.378667	0.12	860	0.4	860	0.3	0.84	0.01	9.755	0.002	58.8	0.71	0.01	7.723	0.001	57.7
IRAS06108	92.544704	-70.767581	92.544510	-70.767579	0.25	527	0.3	528	0.3	0.54	0.01	10.179	0.003	34.2	0.46	0.01	8.512	0.002	31.1
IRAS05506	87.485502	-70.886597	87.485630	-70.886601	0.17	1029	1.6	1018	1.3	0.77	0.02	9.416	0.006	141.5	0.70	0.02	7.563	0.005	129.8
IRAS05125	78.003364	-70.540098	78.003233	-70.540035	0.28	1147	1.4	1147	1.4	0.67	0.01	11.073	0.005	54.5	0.55	0.01	8.522	0.004	58.4
ERO0529379	82.407854	-72.831365	82.407960	-72.831345	0.22	685	1.4	686	1.7	0.54	0.02	14.179	0.010	20.7	0.50	0.03	10.793	0.009	131.5
ERO0518117	79.548769	-70.507508	79.548787	-70.507469	0.32	9479	406.5	7935	143.5	0.96	0.04	14.598	0.055	15.0	0.99	0.03	11.471	0.024	16.2

Notes. Listed are the source name, the input coordinates used to search the WISE/NEOWISE archive, the "final" coordinates being the average of the coordinates of all entries contributing to the LC, the distance between input and final coordinates, periods in the W1 and W2 band, the amplitude, mean magnitude and reduced χ^2 in the W1 band, the amplitude, mean magnitude and reduced χ^2 in the W2 band. All error bars have been scaled to give a reduced χ^2 of unity.

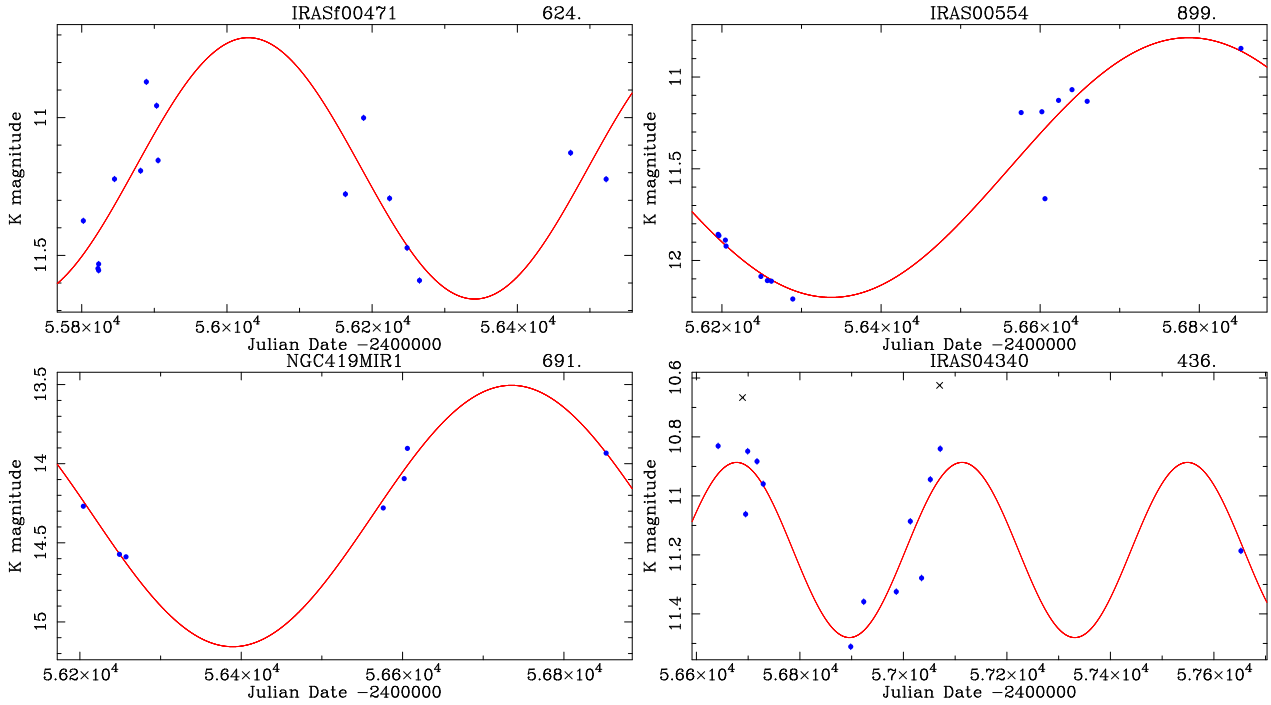

Fig. C.1: Examples of the LC and the model fit (in red) in the *K*-band. A cross indicates a data point is excluded from the fit. The source name and period are listed at the top of the plot. The complete set of figures is available via Zenodo.

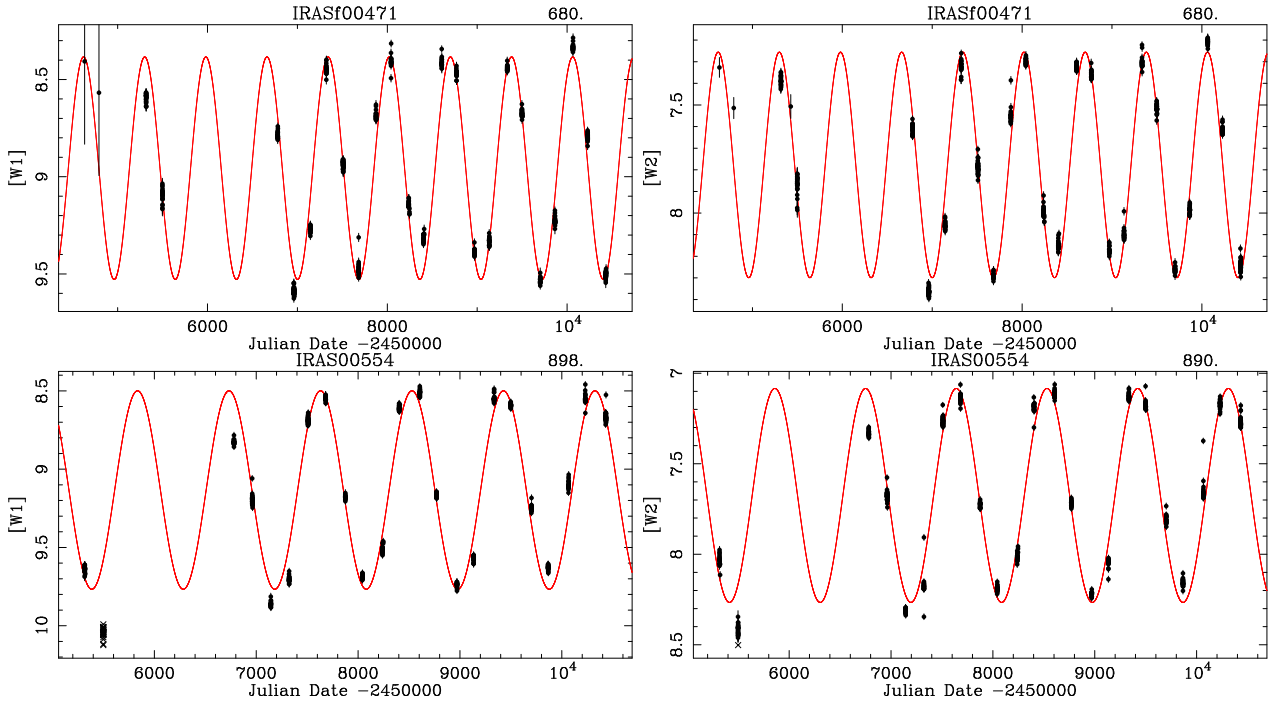

Fig. C.2: Examples of the LC and the model fit (in red) in the W1-band (left panel), and W2-band (right panel) for the same stars as in Fig. C.1. The complete set of figures is available via Zenodo.

Appendix D: SED fitting

Table D.1 gives the references to the photometric data used to construct the SEDs.

Input to the MoD RT models are atmosphere models from Aringer et al. (2009) with Z/Z$_\odot$= 0.10 and 0.33 for the SMC and LMC, respectively, $T_{\rm eff}$ between 2600 and 4000 K at 100 K intervals, $\log g$ =0.0 dex, and a fixed C/O ratio of 1.4 and mass of 2 M$_\odot$. These abundances in the Aringer model grid are closest to the SMC and LMC abundances. The photometry is de-reddened using the reddening map of Skowron et al. (2021) and the $E(V-I)$ value in that map closest to the source is taken. The visual extinction is then adopted as $A_{\rm V} = 3.1 \cdot E(V-I)/1.318$, following Skowron et al. (2021), and the reddening law of Cardelli et al. (1989) is used with $R_{\rm V}$= 3.1 at other wavelengths.

The dust around the C stars is assumed to be a combination of AMC, SiC, and MgS. The optical constants are taken from Zubko et al. (1996) (the ACAR species) for AMC, Pitman et al. 2008 for SiC, and Hofmeister et al. (2003) for MgS. The absorption and scattering coefficients are calculated using a distribution of hollow spheres (DHS, Min et al. 2005) with assuming a typical grain size of 0.15 μm. In DHS, the grains are modelled with a vacuum core which has a fractional volume uniformly distributed between zero and $f_{\rm max}$ in order to simulate the fluffiness of real grains. Groenewegen & Sloan (2018) found that $f_{\rm max}$ = 0.7 fitted the data well, and we use that value here. SiC and MgS are minor species relative to AMC, and the specific density of the dust grains is around 1.5 g cm^{-3}[8].

In the Nanni models the formation of AMC, SiC, and metallic iron dust species are considered. The input optical properties and typical grain size for amorphous carbon dust have been selected to reproduce the colour-colour diagrams in the infrared and colour-magnitude diagrams based on a combination of 2MASS and *Gaia* DR2 photometry (see Lebzelter et al. 2018; Nanni et al. 2016; Nanni 2019). The optical properties of AMC, SiC and metallic iron are from Jäger et al. (1998), Pégourié (1988) and Leksina & Penkina (1967), respectively.

Figure D.1 shows examples of the fits to the SEDs. On the left side the MoD models and on the right side the Nanni models for a given star. The complete set of figures is available via Zenodo.

Figure D.2 compares MLRs, luminosities and GTD ratios between the two sets of RT models. These models have been run independently and are run under slightly different assumptions. For example, different optical properties of AMC and SiC have been adopted and different grain geometries (solid spheres versus a distribution of hollow spheres). MgS is considered in MoD (but not metallic iron) and vice versa for the Nanni models. The Nanni models fit only the observed photometry, while in the MoD models the mid-IR spectrum (when available) is also part of the fit and used to manually adjust the fractions of SiC and MgS relative to AMC. In MoD the temperature at the inner dust radius is allowed to vary freely, while in the Nanni models the dust formation and condensation process is followed self-consistently which implies typically values close to the expected condensation temperature. In the Nanni models the luminosity is not fit freely, but the best match among a grid of luminosities is chosen.

Star symbols in Fig. D.2 indicate unreliable models and excludes stars with either poor fits to the SEDs (defined as the poorest 10% in χ^2 in either the Nanni or MoD models), or very low dust temperatures at the inner radius (below 700 K in either the Nanni or MoD models), so that the hypothesis of a dust driven wind is likely not directly applicable).

Table D.1: Photometry used to construct the SEDs.

Filters	Instrument	Reference
V, I	OGLE	Soszyński et al. (2009, 2011)
$B_{\rm p}, G, R_{\rm p}$	*Gaia*	Gaia Collaboration (2023)
Y, J, K	VMC DR6	Cioni et al. (2011)
J, H, K	2MASS-6X	Cutri et al. (2012)
J, H, K	IRSF	Kato et al. (2007)
S7, S11, L15[b]	Akari	Ita et al. (2010); Kato et al. (2012)
9, 18 μm	Akari	Ishihara et al. (2010)
W1, W2, W3, W4[c]	AllWISE	Cutri & et al. (2014)
3.6, 4.5, 5.8, 8.5 μm	*Spitzer* IRAC	IPAC[d], Gruendl et al. (2008); Whitney et al. (2008)
A,C,D	MSX	Egan et al. (2003)
12, 25 μm	IRAS PSC & FSC	Beichmann (1985); Moshir et al. (1993)
24, 70 μm	*Spitzer* MIPS	IRSA[e], Gruendl et al. (2008)
70 – 350 μm	*Herschel* PACS, SPIRE	Seale et al. (2014)
1330 μm	ALMA	This work
4.5, 6.7, 12 μm	ISOCAM	Tanabé et al. (2004), for NGC419 MIR1

Notes. [(a)]For the S7, S11, and L15 filters only errors in the magnitudes of <0.15, <0.20, and <0.20 mag were accepted, respectively; [(b)]In the W3 and W4 filters only errors in the magnitudes of <0.30, and <0.25 mag were accepted, respectively; [(c)]VizieR catalog II/305/catalog; [(d)]`https://irsa.ipac.caltech.edu/applications/Gator/`, the "SAGE MIPS 24 um Epoch 1 and Epoch 2 Full List".

[8] $\rho_{\rm d}$ is 1.50 g cm^{-3} for a mix AMC:SiC:MgS=100:5:10 which was adopted in 27 objects, and the density ranges from 1.30 g cm^{-3} for pure AMC (adopted in 2 sources) to 1.66 g cm^{-3}, adopted in one source.

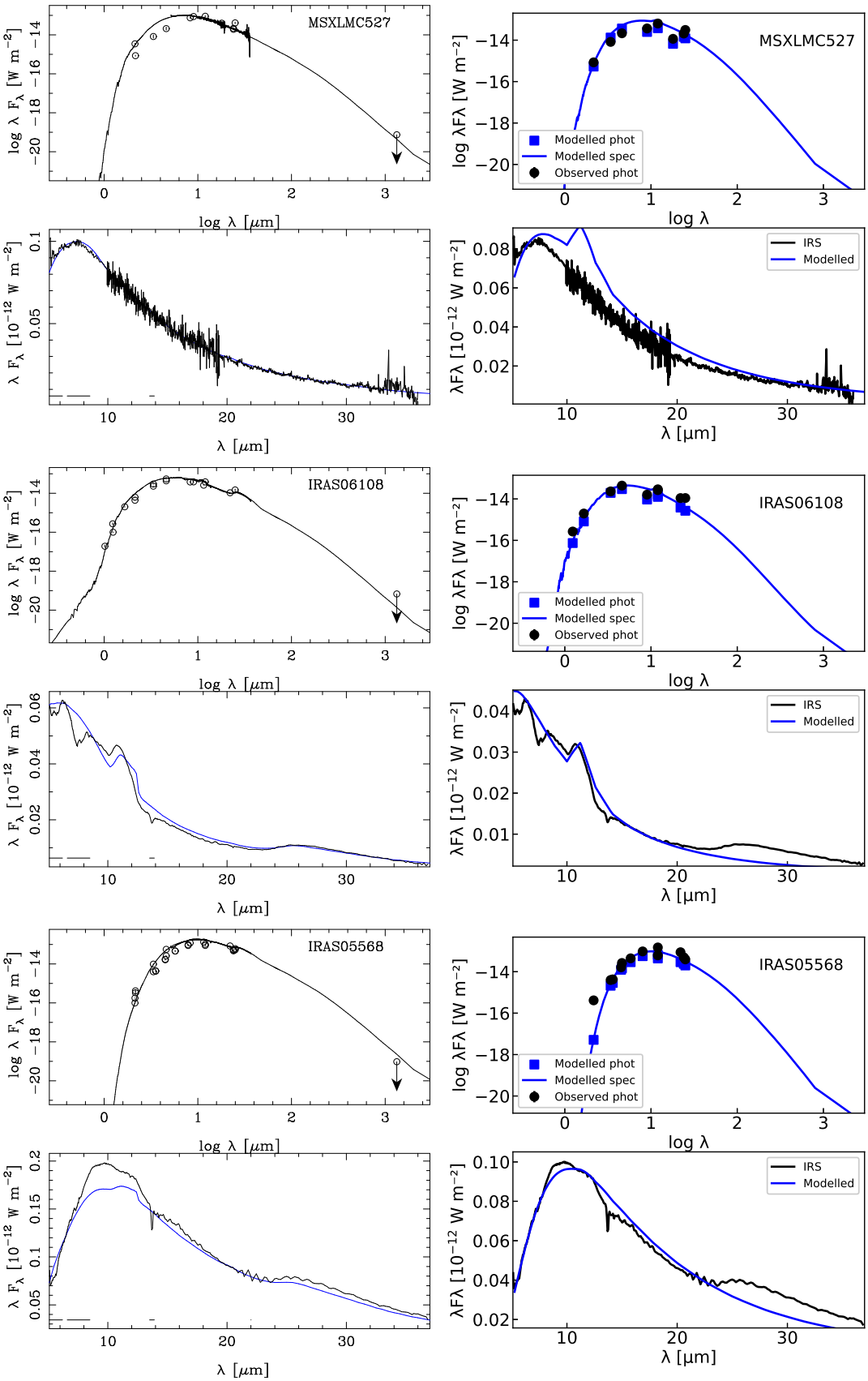

Fig. D.1: Examples of SED fits. On the left the MoD models and on the right the Nanni models. In the MoD models the model spectra are scaled to match the observed spectra based on the average flux in the 6.35–6.55 μm region, in the Nanni models the spectra are not included in the fitting, but the scaling is applied. The complete set of figures is available via Zenodo.

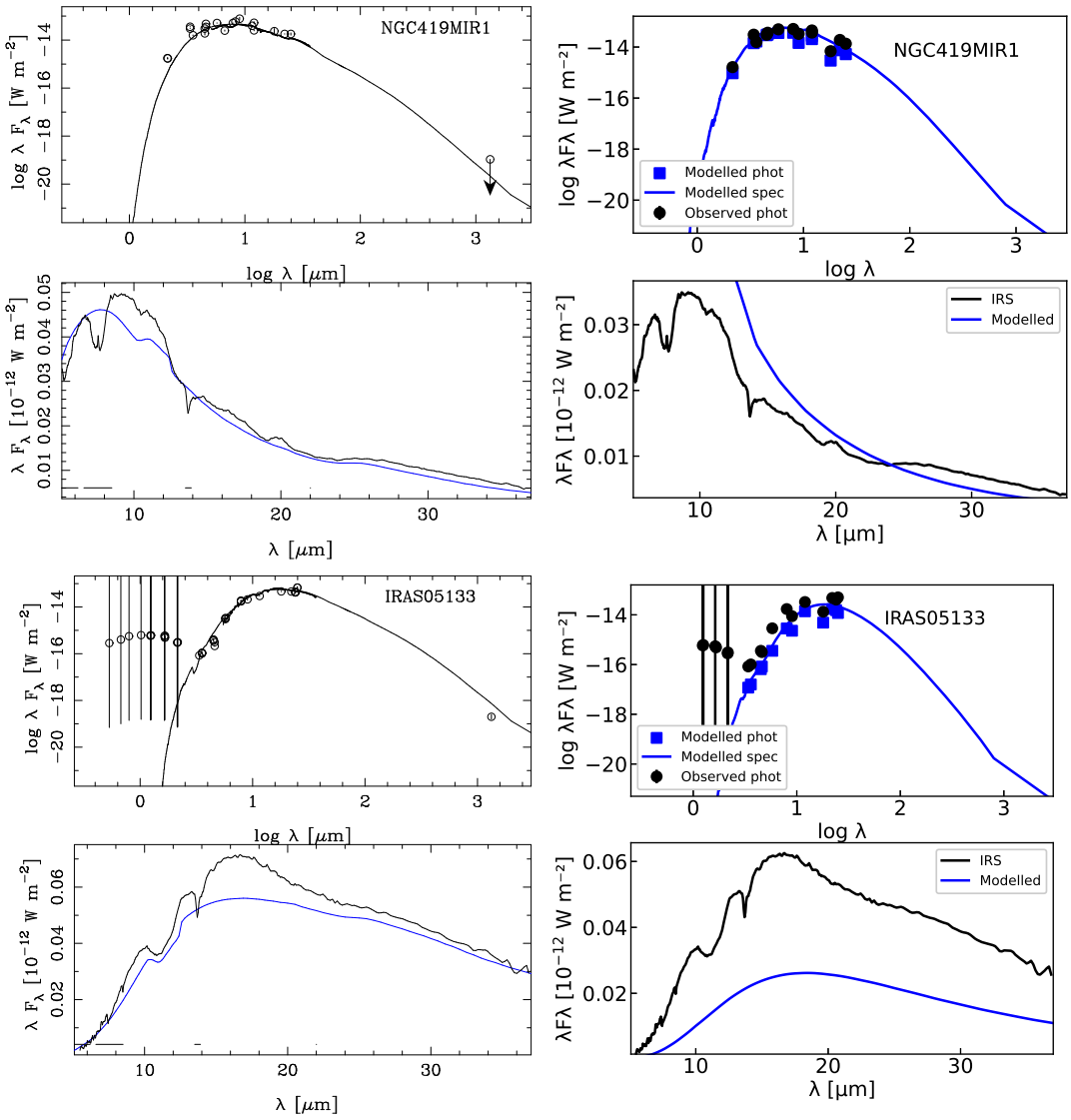

Fig. D.1: continued.

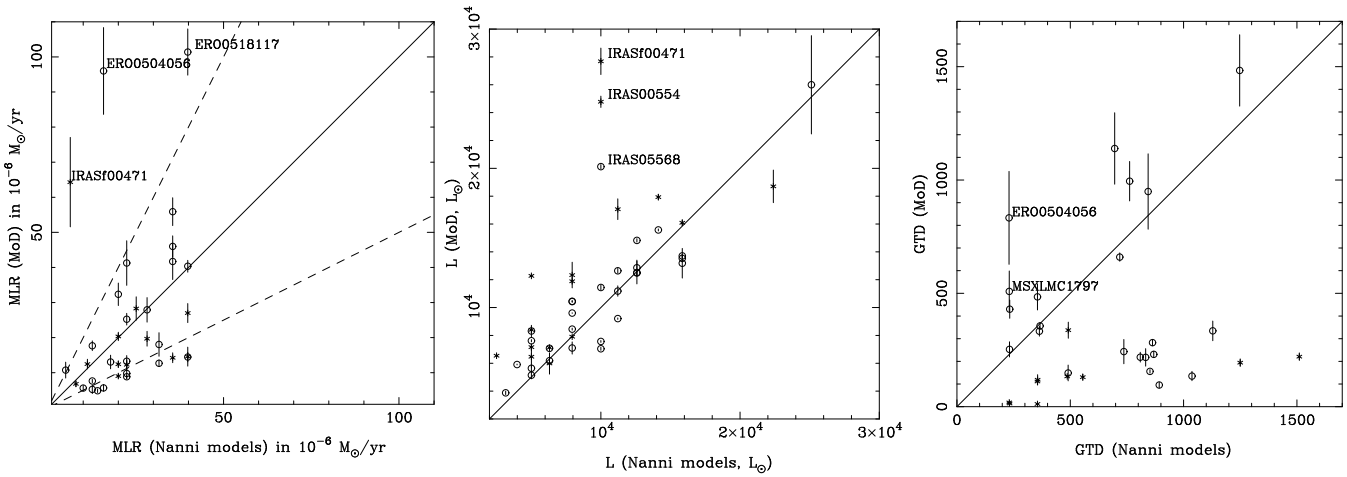

Fig. D.2: Comparison of the fitting results from MoD and the Nanni models for the MLR (left), luminosity (middle), and GTD ratio (right-hand panel). The one-to-one line is drawn in all panels, and in the two left-most panels lines that indicate factors of 0.5 and 2 difference as well. Outliers are labelled. Star symbols indicate unreliable models (see text in Appendix D).

Appendix E: Additional tables

Table E.1: Results of the ALMA observations.

Name	SG	RA (h:m:s)	Dec (d:m:s)	Source size (″)	Continuum (mJy)	Area (Jy km s^{-1})	$V_\star$ (km s^{-1})	ΔV (km s^{-1})	Peak (Jy)	RMS (Jy)	Area (Jy km/s)	RMS (Jy)
IRASf00471	SMC	0:48:59.491 ± 0.024	-73:35:38.832 ± 0.035	0.475 ± 0.083 x 0.398 ± 0.056	< 0.039	0.169 ± 0.032	171.66 ± 0.65	13.40 ± 1.86	0.019 ± 0.003	0.007	< 0.093	0.007
IRAS00554	SMC	[a]			< 0.036	< 0.115	170.00 f	18.00 f	< 0.010	0.007	< 0.096	0.007
NGC419MIR1	SMC	1:08:17.479 ± 0.023	-72:53:09.413 ± 0.023	0.658 ± 0.059 x 0.587 ± 0.048	< 0.048	0.586 ± 0.033	174.08 ± 0.32	19.82 ± 0.82	0.044 ± 0.003	0.007	< 0.096	0.006
IRAS04340	LMCwk	4:33:43.766 ± 0.179	-70:09:50.573 ± 0.066	1.168 ± 0.422 x 0.672 ± 0.154	< 0.027	0.147 ± 0.033	251.49 ± 0.98	21.39 ± 2.95	0.010 ± 0.002	0.005	< 0.060	0.004
IRAS04375	LMCst	4:36:44.503 ± 0.035	-72:42:01.051 ± 0.046	0.804 ± 0.111 x 0.664 ± 0.079	0.122 ± 0.027	1.073 ± 0.117	244.27 ± 1.52	44.54 ± 4.90	0.036 ± 0.004	0.015	< 0.315	0.015
MSXLMC1119	LMCwk	4:47:38.848 ± 0.050	-69:21:16.981 ± 0.060	1.066 ± 0.163 x 0.755 ± 0.087	0.077 ± 0.011	0.559 ± 0.038	253.69 ± 0.74	37.52 ± 1.84	0.022 ± 0.002	0.005	< 0.135	0.006
IRAS04496	LMCwk	[a]			< 0.039	< 0.029	250.00 f	30.00 f	< 0.001	0.005	< 0.084	0.005
IRAS04523	LMCwk	4:51:50.919 ± 0.017	-70:38:32.064 ± 0.019	0.937 ± 0.051 x 0.752 ± 0.034	< 0.045	1.513 ± 0.038	221.64 ± 0.26	35.86 ± 0.80	0.063 ± 0.002	0.008	< 0.141	0.005
SAGEMCJ045344	LMCst	[a]			< 0.195	< 0.504	250.00 f	30.00 f	< 0.025	0.016	< 0.258	0.014
IRAS04557	LMCst	4:55:38.981 ± 0.026	-67:49:10.528 ± 0.015	0.628 ± 0.062 x 0.469 ± 0.034	< 0.072	1.413 ± 0.132	293.28 ± 1.15	38.90 ± 3.32	0.054 ± 0.004	0.016	< 0.432	0.017
MSXLMC1220	LMCwk	[a]			< 0.033	< 0.143	250.00 f	30.00 f	< 0.007	0.006	< 0.114	0.006
MSXLMC1303	LMCwk	4:58:42.042 ± 0.166	-68:07:15.006 ± 0.049	1.145 ± 0.399 x 0.522 ± 0.086	0.093 ± 0.012	0.275 ± 0.021	248.10 ± 0.33	15.59 ± 0.94	0.026 ± 0.002	0.006	< 0.063	0.005
MSXLMC1282	LMCwk	5:01:00.900 ± 0.038	-67:35:23.676 ± 0.053	1.162 ± 0.143 x 0.686 ± 0.055	< 0.030	0.667 ± 0.041	241.21 ± 1.26	69.67 ± 3.00	0.014 ± 0.001	0.004	< 0.138	0.005
ERO0502315	LMCst	5:02:31.504 ± 0.202	-68:05:35.880 ± 1.050	2.387 ± 2.474 x 0.691 ± 0.469	< 0.078	1.164 ± 0.094	218.59 ± 0.49	21.56 ± 1.40	0.080 ± 0.006	0.016	< 0.249	0.017
MSXLMC91	LMCst	5:03:38.573 ± 0.055	-68:53:12.710 ± 0.057	0.701 ± 0.135 x 0.682 ± 0.128	< 0.072	2.200 ± 0.122	258.30 ± 0.82	44.20 ± 2.63	0.075 ± 0.004	0.015	< 0.451	0.017
TRM74	LMCwk	5:03:43.012 ± 0.017	-66:44:56.530 ± 0.019	0.916 ± 0.047 x 0.807 ± 0.037	< 0.030	1.442 ± 0.048	280.32 ± 0.26	25.15 ± 1.34	0.086 ± 0.003	0.009	< 0.084	0.005
ERO0504056	LMCst	5:04:05.621 ± 0.037	-68:23:40.312 ± 0.030	0.601 ± 0.086 x 0.536 ± 0.069	< 0.066	0.656 ± 0.089	261.48 ± 0.59	14.88 ± 1.76	0.066 ± 0.008	0.017	< 0.237	0.016
MSXLMC87	LMCwk	5:10:19.656 ± 0.053	-69:49:51.506 ± 0.075	1.042 ± 0.179 x 0.837 ± 0.121	0.080 ± 0.008	0.696 ± 0.051	230.56 ± 1.62	69.20 ± 4.27	0.015 ± 0.001	0.005	< 0.195	0.005
IRAS05113	LMCwk	5:10:56.854 ± 0.033	-69:35:30.512 ± 0.049	0.952 ± 0.118 x 0.747 ± 0.075	< 0.030	0.522 ± 0.045	217.20 ± 2.47	66.98 ± 7.39	0.012 ± 0.001	0.005	< 0.152	0.005
IRAS05132	LMCwk	5:12:51.062 ± 0.025	-69:37:50.351 ± 0.032	0.970 ± 0.084 x 0.714 ± 0.047	0.035 ± 0.008	0.874 ± 0.038	255.15 ± 0.39	39.62 ± 1.11	0.033 ± 0.001	0.008	< 0.111	0.005
IRAS05133	LMCst	5:13:01.786 ± 0.025	-69:33:50.951 ± 0.025	0.605 ± 0.067 x 0.518 ± 0.049	0.088 ± 0.024	1.071 ± 0.096	227.27 ± 0.75	26.12 ± 3.34	0.061 ± 0.005	0.014	< 0.292	0.015
ERO0518484	LMCst	5:18:48.404 ± 0.031	-69:33:34.650 ± 0.041	0.577 ± 0.098 x 0.497 ± 0.072	< 0.078	0.412 ± 0.087	237.98 ± 0.60	16.05 ± 1.50	0.037 ± 0.008	0.014	< 0.213	0.017
IRAS05190	LMCwk	5:18:56.271 ± 0.010	-67:45:04.475 ± 0.010	0.854 ± 0.026 x 0.754 ± 0.021	< 0.030	2.354 ± 0.043	236.70 ± 0.23	37.84 ± 0.86	0.093 ± 0.002	0.008	< 0.123	0.006
TRM88	LMCwk	5:20:19.410 ± 0.066	-66:35:47.854 ± 0.039	0.864 ± 0.159 x 0.639 ± 0.087	< 0.036	0.344 ± 0.044	260.55 ± 2.13	62.05 ± 7.51	0.008 ± 0.001	0.005	< 0.144	0.006
MSXLMC527	LMCwk	[a]			< 0.033	< 0.176	290.00 f	30.00 f	< 0.009	0.007	< 0.110	0.005
ERO0525406	LMCst	5:25:40.655 ± 0.035	-70:08:27.244 ± 0.040	0.594 ± 0.111 x 0.424 ± 0.055	< 0.102	0.498 ± 0.091	227.86 ± 1.06	17.41 ± 2.94	0.041 ± 0.010	0.015	< 0.300	0.016
MSXLMC474	LMCst	[a]			< 0.069	< 0.399	250.00 f	30.00 f	< 0.020	0.015	< 0.375	0.017
IRAS05315	LMCst	5:30:44.134 ± 0.019	-71:43:00.509 ± 0.019	0.612 ± 0.046 x 0.607 ± 0.045	< 0.072	1.594 ± 0.088	239.74 ± 0.43	25.03 ± 1.26	0.096 ± 0.006	0.015	< 0.243	0.013
MSXLMC1780	LMCwk	5:33:01.796 ± 0.033	-68:23:58.434 ± 0.038	1.097 ± 0.089 x 1.011 ± 0.078	0.055 ± 0.011	1.653 ± 0.143	256.76 ± 1.00	31.70 ± 3.08	0.078 ± 0.004	0.015	< 0.189	0.006
IRAS05373	LMCst	5:36:24.161 ± 0.026	-72:41:32.604 ± 0.037	0.704 ± 0.089 x 0.572 ± 0.060	< 0.099	1.078 ± 0.106	210.73 ± 0.73	27.25 ± 2.24	0.059 ± 0.005	0.016	< 0.222	0.014
MSXLMC971	LMCwk	5:39:51.840 ± 0.035	-70:01:17.134 ± 0.037	0.992 ± 0.098 x 0.820 ± 0.069	< 0.027	0.910 ± 0.034	254.24 ± 0.26	28.79 ± 0.66	0.047 ± 0.002	0.006	< 0.115	0.005
MSXLMC937	LMCwk	5:40:36.105 ± 0.038	-69:52:49.901 ± 0.049	1.095 ± 0.130 x 0.765 ± 0.068	< 0.021	0.854 ± 0.055	260.60 ± 0.46	50.35 ± 1.98	0.025 ± 0.002	0.006	< 0.120	0.006
IRAS05416	LMCwk	5:41:20.757 ± 0.015	-69:04:43.723 ± 0.024	0.873 ± 0.057 x 0.679 ± 0.035	< 0.039	1.300 ± 0.033	236.04 ± 0.25	27.85 ± 0.87	0.070 ± 0.002	0.005	< 0.084	0.005
LMCLPV76711	LMCwk	5:42:17.234 ± 0.099	-70:32:20.292 ± 0.099	1.121 ± 0.295 x 0.758 ± 0.148	< 0.030	0.253 ± 0.048	255.54 ± 1.62	26.58 ± 5.62	0.014 ± 0.002	0.006	< 0.099	0.006
IRAS05495	LMCst	5:49:00.004 ± 0.014	-70:33:22.489 ± 0.017	0.657 ± 0.040 x 0.595 ± 0.033	0.116 ± 0.019	2.275 ± 0.109	246.85 ± 0.42	31.43 ± 1.23	0.109 ± 0.005	0.016	< 0.336	0.016
ERO0550261	LMCst	5:50:26.131 ± 0.019	-69:56:03.066 ± 0.022	0.723 ± 0.056 x 0.580 ± 0.037	< 0.111	1.828 ± 0.104	270.39 ± 0.67	31.39 ± 2.05	0.087 ± 0.005	0.015	< 0.300	0.015
IRAS05515	LMCst	5:50:49.947 ± 0.034	-71:23:35.567 ± 0.041	0.770 ± 0.102 x 0.645 ± 0.074	< 0.099	1.536 ± 0.091	243.00 ± 0.77	41.52 ± 2.07	0.056 ± 0.004	0.013	< 0.309	0.015
MSXLMC1797	LMCwk	5:51:33.584 ± 0.098	-71:19:34.298 ± 0.119	1.260 ± 0.317 x 0.884 ± 0.177	0.114 ± 0.012	0.550 ± 0.034	249.45 ± 0.33	19.04 ± 1.42	0.043 ± 0.002	0.005	< 0.084	0.006
IRAS05568	LMCwk	5:56:38.769 ± 0.015	-67:53:33.896 ± 0.023	0.949 ± 0.055 x 0.738 ± 0.034	< 0.042	1.498 ± 0.033	267.28 ± 0.19	28.20 ± 0.56	0.080 ± 0.002	0.008	[b]	0.006
IRAS06028	LMCst	6:02:45.136 ± 0.020	-67:22:43.151 ± 0.020	0.610 ± 0.048 x 0.604 ± 0.047	< 0.111	1.898 ± 0.122	281.52 ± 0.71	40.58 ± 1.90	0.070 ± 0.004	0.015	< 0.354	0.017
IRAS06108	LMCwk	6:10:10.729 ± 0.064	-70:46:03.292 ± 0.066	0.937 ± 0.171 x 0.816 ± 0.133	< 0.030	0.476 ± 0.031	256.93 ± 0.34	18.76 ± 0.95	0.038 ± 0.002	0.006	< 0.090	0.006

Notes. Listed are the source name, the SG (see Tab. 1), the fitted coordinates with errors from the ALMA image (Fig. A.1), the major and minor axis of the source size (not deconvolved with the beam), the continuum flux at 1330 μm and error, the integrated area of the ^{12}CO emission with error, the stellar velocity with error, the full width at zero intensity of the ^{12}CO profile with error, the peak intensity of the profile with error, the rms noise level, the upper limit to the integrated area of the ^{13}CO emission, and the rms level.

[a] Input coordinates (Ra, Dec) of the objects that were not detected: IRAS 00554 (0:57:03.928, −73:35:14.593), IRAS 04496 (4:49:18.460, −69:53:14.494), SAGEMCJ045344 (4:53:44.280, −66:11:45.953), MSXLMC1220 (4:55:41.779, −68:57:22.621), MSXLMC527 (5:22:19.740, −65:43:18.898), MSXLMC474 (5:25:51.840, −68:46:34.207), [b] IRAS 05568 was detected in ^{13}CO with an integrated intensity 0.81 ± 0.04 Jy km s^{-1}, $V_\star$ = 267.33 ± 0.35 km s^{-1}, and a peak of 0.043 ± 0.002 Jy (for a fixed $V_{\rm exp}$ of 14.1 km s^{-1}).

Table E.2: Results of the SED modelling and adopted pulsation periods.

Name	L ($L_\odot$)	GTD	$\dot{M}\times10^6$ ($M_\odot$ yr^{-1})	V (km s^{-1})	T_c (K)	L ($L_\odot$)	GTD	$\dot{M}\times10^6$ ($M_\odot$ yr^{-1})	T_c (K)	L ($L_\odot$)	GTD	$\dot{M}\times10^6$ ($M_\odot$ yr^{-1})	$\dot{M}\times10^6$ ($M_\odot$ yr^{-1})	Period (d)
	Nanni models					MoD				Adopted			CO model	
IRASf00471	10000	1889	6.3	8.1	1164	27685 ± 950	9690 ± 2973	64.3 ± 12.7	1107 ± 17	16639	4279	20	9.6	680.0 ± 0.6
IRAS00554	10000	1109	11.2	15.0	1051	24779 ± 405	2072 ± 1373	43.5 ± 15.1	865 ± 10	15741	1516	22	< 8.0	893.2 ± 0.7
NGC419MIR1	10000	762	22.4	10.8	1013	7566 ± 68	995 ± 87	25.3 ± 1.7	1000 F	8698	871	24	32.0	717.8 ± 0.5
IRAS04340	5012	1670	5.0	7.3	1164	8314 ± 411	2409 ± 756	10.7 ± 2.3	1116 ± 24	6455	2006	7	5.1	439.6 ± 0.3
IRAS04375	10000	491	15.8	21.7	999	7040 ± 112	149 ± 35	5.7 ± 1.0	805 ± 14	8391	270	9	36.5	693.8 ± 0.4
MSXLMC1119	7943	1129	10.0	17.1	1061	7095 ± 437	334 ± 43	5.6 ± 0.8	906 ± 43	7507	614	7	19.8	544.4 ± 0.2
IRAS04496	25120	1885	15.8	26.0	1166	25999 ± 3529	686 ± 853	18.7 ± 13.2	708 ± 44	25556	1137	17	< 1.6	
IRAS04523	22390	1511	35.5	18.6	1046	18705 ± 1171	221 ± 17	14.3 ± 1.4	665 ± 29	20465	577	23	43.8	874.4 ± 0.5
SAGEMCJ045344	7943	973	17.8	4.0	1001	8451 ± 74	249 ± 285	14.9 ± 7.9	800 ± 14	8193	493	16	< 16.4	761.0 ± 0.3
IRAS04557	12590	833	22.4	14.8	1003	14824 ± 121	217 ± 39	13.3 ± 1.6	746 ± 9	13662	426	17	43.0	729.7 ± 0.3
MSXLMC1220	5012	1629	3.2	4.0	1244	6471 ± 761	477 ± 586	5.6 ± 3.8	862 ± 90	5695	881	4	< 5.8	513.7 ± 0.3
MSXLMC1303	11220	696	35.5	8.9	999	11186 ± 373	1139 ± 158	41.7 ± 5.1	838 ± 21	11203	890	38	7.4	1005.0 ± 3.1
MSXLMC1282	11220	555	7.9	35.1	1052	17063 ± 745	130 ± 14	6.8 ± 0.8	851 ± 13	13837	269	7	30.4	608.5 ± 0.5
ERO0502315	7943	355	39.8	9.8	892	7910 ± 65	111 ± 15	27.0 ± 2.7	554 ± 10	7926	199	33	28.0	
MSXLMC91	12590	1037	22.4	21.3	1033	12516 ± 817	135 ± 21	9.8 ± 1.6	705 ± 35	12553	374	15	65.6	897.0 ± 0.5
TRM74	5012	231	22.4	10.9	893	7160 ± 228	19 ± 2	12.3 ± 1.4	318 ± 12	5990	65	17	35.8	
ERO0504056	3981	230	15.8	5.9	898	5911 ± 31	833 ± 205	96.0 ± 12.4	1000 F	4851	438	39	14.7	
MSXLMC87	15850	892	14.1	34.0	1133	13536 ± 270	96 ± 13	4.9 ± 0.5	764 ± 12	14647	292	8	31.4	615.4 ± 1.2
IRAS05113	15850	555	12.6	39.8	1044	13183 ± 1062	81 ± 22	5.3 ± 1.2	733 ± 43	14455	212	8	24.4	630.6 ± 0.7
IRAS05132	11220	868	22.4	18.5	1011	9207 ± 54	231 ± 14	8.8 ± 0.5	835 ± 8	10164	448	14	29.3	681.7 ± 0.4
IRAS05133	2512	118	39.8	8.3	363	6544 ± 89	42 ± 11	14.6 ± 2.7	449 ± 12	4054	70	24	28.5	
ERO0518484	6310	356	28.2	5.8	908	7118 ± 14	119 ± 23	19.7 ± 2.1	430 ± 3	6702	205	24	10.4	803.0 ± 22.3
IRAS05190	12590	852	31.6	19.5	1001	12482 ± 130	156 ± 8	12.7 ± 0.9	705 ± 12	12536	364	20	64.6	953.1 ± 0.9
TRM88	7943	490	7.9	34.0	1040	12334 ± 921	315 ± 91	4.5 ± 1.3	1000 F	9898	393	6	16.7	536.7 ± 0.4
MSXLMC527	10000	1020	20.0	4.0	1047	11444 ± 173	424 ± 486	18.5 ± 10.7	886 ± 25	10698	658	19	< 6.9	
ERO0525406	3162	356	17.8	5.6	908	3873 ± 125	220 ± 82	23.3 ± 7.1	712 ± 46	3500	280	20	12.6	
MSXLMC474	11220	1447	11.2	8.2	1081	12641 ± 169	498 ± 571	12.5 ± 6.5	837 ± 10	11910	849	12	< 13.5	622.8 ± 0.4
IRAS05315	5012	232	20.0	11.4	901	8399 ± 37	14 ± 1	12.4 ± 1.0	266 ± 3	6488	57	16	38.8	
MSXLMC1780	12590	737	31.6	11.5	975	12857 ± 553	243 ± 53	18.0 ± 3.4	737 ± 29	12723	423	24	44.5	847.9 ± 0.5
IRAS05373	6310	844	17.8	15.9	1051	7072 ± 118	949 ± 166	13.0 ± 1.9	1163 ± 29	6680	895	15	29.3	643.7 ± 0.5
MSXLMC971	6310	863	12.6	13.4	1021	6184 ± 53	283 ± 14	7.6 ± 0.5	766 ± 10	6247	494	10	26.1	648.6 ± 0.3
MSXLMC937	15850	1250	20.0	22.9	1125	16091 ± 203	194 ± 17	9.0 ± 0.6	816 ± 6	15970	493	13	32.1	691.0 ± 0.6
IRAS05416	7943	364	28.2	12.9	941	10451 ± 65	333 ± 22	27.9 ± 3.5	879 ± 42	9111	348	28	34.5	904.0 ± 0.6
LMCLPV76711	6310	1272	4.0	9.2	1193	5988 ± 766	486 ± 260	5.8 ± 2.5	807 ± 84	6147	786	5	8.8	550.8 ± 0.3
IRAS05495	5012	355	20.0	4.0	931	12277 ± 61	12 ± 1	20.3 ± 1.2	311 ± 3	7844	65	20	57.6	
ERO0550261	7943	232	35.5	16.2	884	10426 ± 32	253 ± 34	55.9 ± 4.0	1000 F	9100	242	45	48.2	1111.8 ± 1.2
IRAS05515	7943	491	11.2	19.5	1006	11890 ± 130	337 ± 36	12.5 ± 1.4	963 ± 21	9718	407	12	47.5	666.1 ± 0.3
MSXLMC1797	5012	231	22.4	10.0	912	5144 ± 266	509 ± 90	41.3 ± 6.4	1000 F	5078	343	30	14.3	698.8 ± 1.2
IRAS05568	10000	366	35.5	14.8	922	20119 ± 153	356 ± 16	46.0 ± 3.0	798 ± 16	14184	361	40	38.9	1207.0 ± 0.7
IRAS06028	15850	809	39.8	18.6	984	13708 ± 125	218 ± 22	14.5 ± 1.4	813 ± 15	14740	420	24	55.9	860.0 ± 0.2
IRAS06108	5012	1248	12.6	10.7	1041	7617 ± 81	1483 ± 157	17.7 ± 1.4	1000 F	6179	1360	15	12.6	527.5 ± 0.2
IRAS05506	14130	486	25.1	24.5	1021	17934 ± 196	134 ± 5	28.3 ± 3.3	1095 ± 57	15919	255	27	28.4	1022.4 ± 1.0
IRAS05125	14130	718	39.8	12.1	968	15574 ± 74	660 ± 18	40.3 ± 1.7	869 ± 11	14834	689	40	8.1	1147.1 ± 1.0
ERO0529379	5012	233	20.0	11.4	929	5638 ± 216	430 ± 40	32.4 ± 3.2	1000 F	5316	316	25	7.3	685.4 ± 1.1
ERO0518117	7943	355	39.8	9.8	892	9604 ± 22	484 ± 58	101.4 ± 6.6	900 F	8734	415	64	7.4	